Episodes of particle ejection from the surface of the active asteroid (101955) Bennu

Version: Accepted Manuscript

Link(s) to article on publisher's website:
http://dx.doi.org/doi:10.1126/science.aay3544

Episodes of particle ejection from the surface of the active asteroid (101955) Bennu

D. S. Lauretta[1]*†, C. W. Hergenrother[1]*†, S. R. Chesley[2], J. M. Leonard[3], J. Y. Pelgrift[3], C. D. Adam[3], M. Al Asad[4], P. G. Antreasian[3], R.-L. Ballouz[1], K. J. Becker[1], C. A. Bennett[1], B. J. Bos[5], W. F. Bottke[6], M. Brozović[2], H. Campins[7], H. C. Connolly Jr.[8,1], M. G. Daly[9], A. B. Davis[10], J. de León[11], D. N. DellaGiustina[1,12], C. Y. Drouet d'Aubigny[1], J. P. Dworkin[5], J. P. Emery[13,14], D. Farnocchia[2], D. P. Glavin[5], D. R. Golish[1], C. M. Hartzell[15], R. A. Jacobson[2], E. R. Jawin[16], P. Jenniskens[17], J. N. Kidd Jr.[1], E. J. Lessac-Chenen[3], J.-Y. Li[18], G. Libourel[19], J. Licandro[11], A. J. Liounis[5], C. K. Maleszewski[1], C. Manzoni[20], B. May[20], L. K. McCarthy[3], J. W. McMahon[10], P. Michel[19], J. L. Molaro[18], M. C. Moreau[5], D. S. Nelson[3], W. M. Owen Jr.[2], B. Rizk[1], H. L. Roper[1], B. Rozitis[21], E. M. Sahr[3], D. J. Scheeres[10], J. A. Seabrook[9], S. H. Selznick[1], Y. Takahashi[2], F. Thuillet[19], P. Tricarico[18], D. Vokrouhlický[22], C. W. V. Wolner[1]

[1]Lunar and Planetary Laboratory, University of Arizona, Tucson, AZ, USA.

[2]Jet Propulsion Laboratory, California Institute of Technology, Pasadena, CA, USA.

[3]KinetX Aerospace, Simi Valley, CA, USA.

[4]Department of Earth, Ocean and Atmospheric Sciences, University of British Columbia, Vancouver, BC, Canada.

[5]NASA Goddard Space Flight Center, Greenbelt, MD, USA.

[6]Southwest Research Institute, Boulder, CO, USA.

[7]Department of Physics, University of Central Florida, Orlando, FL, USA.

[8]Department of Geology, Rowan University, Glassboro, NJ, USA.

[9]The Centre for Research in Earth and Space Science, York University, Toronto, ON, Canada.

[10]Smead Department of Aerospace Engineering Sciences, University of Colorado, Boulder, CO, USA.

[11]Instituto de Astrofísica de Canarias and Departamento de Astrofísica, Universidad de La Laguna, Tenerife, Spain.

[12]Department of Geosciences, University of Arizona, Tucson, AZ, USA.

[13]Department of Earth and Planetary Sciences, University of Tennessee, Knoxville, TN, USA.

[14]Northern Arizona University, Flagstaff, AZ, USA.

[15]Department of Aerospace Engineering, University of Maryland, College Park, MD, USA.

[16]Smithsonian Institution National Museum of Natural History, Washington, DC, USA.

[17]SETI (Search for Extraterrestrial Intelligence) Institute, Mountain View, CA, USA.

[18]Planetary Science Institute, Tucson, AZ, USA.

[19]Université Côte d'Azur, Observatoire de la Côte d'Azur, CNRS (Centre national de la recherche scientifique), Laboratoire Lagrange, Nice, France.

[20]London Stereoscopic Company, London, UK.

[21]School of Physical Sciences, Open University, Milton Keynes, UK.

[22]Institute of Astronomy, Charles University, Prague, Czech Republic.

*Corresponding author. Email: lauretta@orex.lpl.arizona.edu (D.S.L.); chergen@lpl.arizona.edu (C.W.H.)

†These authors contributed equally to this work.

Abstract

"Active" asteroids are those that show evidence of ongoing mass loss. We report repeated instances of particle ejection from the surface of (101955) Bennu, demonstrating that it is an active asteroid. The ejection events were imaged by the OSIRIS-REx (Origins, Spectral Interpretation, Resource Identification, and Security–Regolith Explorer) spacecraft. For the three largest observed events, we estimate the ejected particle velocities and sizes, event times, source regions, and energies. We determine the trajectories and photometric properties of several gravitationally bound particles that orbited temporarily in the Bennu environment. We consider multiple hypotheses for the mechanisms leading to particle ejection for the largest events, including rotational disruption, electrostatic lofting, ice sublimation, phyllosilicate dehydration, meteoroid impacts, thermal stress fracturing, and secondary impacts.

One-sentence summary: OSIRIS-REx observed particles ejecting from (101955) Bennu, providing an up-close look at an active asteroid.

Active asteroids are small bodies that have typical asteroidal orbits but show some level of mass-loss activity, such as ejection of dust or the development of a coma or tail (*1*). Several objects in the main asteroid belt or the near-Earth asteroid population have been observed to show varying levels of mass loss, such as the active asteroid 133P/Elst-Pizarro (*2*). Some of these objects behave as comets and eject dust over long periods of time, from days to months, or during multiple perihelion passages [including 133P/Elst-Pizarro (*3*)]. Other active asteroids eject dust over short time scales in one or a series of impulsive events, as in the case of (6478) Gault (*4*). Still others have been observed to split into multiple objects or, in the case of P/2016 G1 (PANSTARRS), completely disintegrate (*5*). Near-Earth asteroid (3200) Phaethon has exhibited low levels of mass loss during multiple orbits when less than 0.15 astronomical units (au) from the Sun (*6*, *7*). Multiple ejection mechanisms have been suggested to explain asteroid activity, including collisions, water-ice sublimation, rotational destabilization, thermal fracturing, and dehydration (*8*).

The OSIRIS-REx (Origins, Spectral Interpretation, Resource Identification, and Security–Regolith Explorer) spacecraft arrived at the ~500-m-diameter B-type near-Earth asteroid (101955) Bennu in December 2018. The OSIRIS-REx Team selected Bennu as the mission target in part on the basis of its spectral similarity to some active asteroids (*9*). We describe and analyze OSIRIS-REx observations of activity originating from Bennu's surface. We first detected this phenomenon in navigational images from 6 January 2019, 1 week after the spacecraft entered orbit and 4 days before Bennu perihelion (*10*). We subsequently detected multiple particle ejection events between December 2018 and February 2019. The largest observed events each released dozens of observed particles.

Particle detections

Dust and natural satellite searches were conducted during the spacecraft's approach to Bennu during early proximity operations in September through November 2018, which yielded null results (*10*). Signs of asteroid activity may have been detected by the OSIRIS-REx Laser Altimeter [OLA (*11*)] (figs. S1 and S2) in December 2018. OLA recorded 21 lidar returns off the limb of the asteroid on 4 days during the Preliminary Survey mission phase at distances 399 m (4 December), 397 m (8 December), and 562 and 576 m (12 December, 3.1 hours apart) from Bennu's center. These signals prompted a search for corresponding objects in imaging data, without success. However, the geometry suggests that these four returns were probably from objects or groups of objects (*12*). Subsequent imaging data showed evidence of particle activity, beginning with a particle 8 ± 3 cm (1σ) in diameter on a suborbital trajectory, observed by the NavCam 1 imager of the Touch and Go Camera System (TAGCAMS) (*13*) on 10 December 2018. We cannot rule out activity before December 2018. The searches performed during the spacecraft's approach to the asteroid did not have sufficient sensitivity to detect most of the activity that was later observed at closer ranges. A particle as large as the one observed on 10 December would have been detectable by the natural satellite searches; lack of detection implies that events ejecting particles of that size were relatively rare or nonexistent during the spacecraft's approach.

On 31 December 2018, the spacecraft entered into an eccentric, near-terminator orbit that ranged between 1.6 and 2.1 km from Bennu's center of mass. This Orbital A mission phase continued until 28 February 2019, when the spacecraft departed orbit to perform the Detailed Survey (*14*).

During the early part of Orbital A, we acquired NavCam 1 image sets roughly every 2 hours to provide optical navigation (OpNav) data for the flight dynamics team (*15*) (table S1). Each image set consisted of four images taken in pairs about 7 minutes apart. Each pair contained a short-exposure image (1.38 ms) to capture landmarks on Bennu's surface, followed immediately by a long-exposure image (5 s) to capture the background star field.

The first particle ejection event that we identified was observed in OpNav images taken on 6 January at 20:56:21 Coordinated Universal Time (UTC) (Fig. 1, A and B, and fig. S3). The particles appear as more than 200 star-like point-source objects and trailed (higher-velocity) objects located off the northern polar limb of Bennu. The second image, taken 7 minutes and 16 seconds later, shows objects in common with the first image that have moved away from Bennu, implying the movement of discrete particles (Fig. 1B). This observation triggered an immediate risk assessment of whether it was safe for the spacecraft to remain in orbit, which was concluded affirmatively, and led to an observational campaign to detect and characterize Bennu's apparent activity.

We increased the imaging cadence in response to the initial event, to better characterize the frequency of particle ejections and any persistent particle population (table S1). Starting on 11 January, NavCam 1 began collecting image pairs of each field every 30 minutes. On 28 January, we again increased the cadence, collecting image pairs of each field every 20 minutes. This imaging frequency continued until 18 February. During this time period, we detected two additional ejection events of a similar scale, on 19 January (Fig. 1, C and D, and fig. S3) and 11 February (fig. S4). The distance from the spacecraft to Bennu's center of mass was 1.66 km for 6

January, 1.99 km for 19 January, and 1.64 km for 11 February. We also observed several smaller events, in which fewer than 20 particles were detected (Fig. 2). There is also a persistent background level of particles in the Bennu environment; we detected a few particles per day during Orbital A, with observed increases immediately following the 19 January and 11 February events (Fig. 2). We use the imaging dataset to characterize these three events, which were the largest observed (i.e., had the highest number of detected particles).

Characterization of the largest observed events

For the 6 January, 19 January, and 11 February events, a particle distribution pattern near the limb of Bennu in the first image is also apparent in the second image collected 7 min later, farther from the limb and dispersed, and also appears in subsequent images for the 19 January and 11 February events. Using OpNav techniques developed for spacecraft navigation, we associate individual particle detections from this pattern and determine the trajectory and velocity of each particle (*12*). Fast-moving particles cross multiple pixels in a single exposure and appear as trails, providing position and velocity information within a single image. For each event, OpNav analysis constrains two possible locations (a near and far radiant) on Bennu's surface from which the particles originated (Table 1, Fig. 3, and table S2) (*12*).

The 6 January event is the least constrained (particles detected in only two images) of the three largest events. We determine that the event originated at a high southern latitude (between about 57˚S and 75˚S; Table 1 and Fig. 3A) (*12*) with an ejection time between 15:22 and 16:35 local solar time (LST). However, the event location relative to the spacecraft and the limited dataset make estimating the precise latitude and ejection time difficult. For this event, we determined

speeds for 117 of the 200 observed particles, ranging from 0.07 to 3.3 m s^{-1}. Fifty-two particles were moving more slowly than Bennu's escape velocity [20 cm s^{-1} for the volume-averaged Bennu radius (*12,16*)] (fig. S5).

Due to the increased imaging cadence, there is a more extensive dataset for the 19 January and 11 February events. We use the output of the OpNav characterization to provide initial conditions for higher-fidelity orbit determination (OD) modeling. In these models, we assume that the particles from a given event left Bennu's surface at the same location on a trajectory influenced by point-mass gravity (*12*). We performed this analysis on 24 particles from the 19 January event (Movie 1) and 25 particles from the 11 February event. For these two events, with individual particles identified in more than three images, this analysis allows us to estimate a single location for the particle source location (Fig. 3, B and C), as well as ejection timing and initial velocity vectors (Table 1).

We determined the ejection epoch (moment in time) by extrapolating the OD solutions backward to the point where they intersect Bennu's surface. This analysis shows that the event on 19 January occurred at 00:53:40.90 ± 3.72 s (3σ) UTC from a location on Bennu at latitude 20˚N, longitude 335˚. The epoch corresponds to 16:38 LST at that location. Surface ejection velocity magnitudes ranged from 0.06 to 1.3 m s^{-1}. The 19 January timing data show a bimodal distribution with a small peak occurring 6 minutes before the main epoch (fig. S6), suggesting that some of the particles may have ejected in a smaller event before the large release. The event on 11 February occurred at 23:27:28.48 ± 6.26 s (3σ) UTC from 20˚N 60˚, corresponding to 18:05 LST, with observed velocity magnitudes ranging from 0.07 to 0.21 m s^{-1}. All particles

from this event appear to have left the surface nearly simultaneously (fig. S6). Many of the characterized particles are on ballistic trajectories that re-impact the surface on the night side of Bennu, while high-velocity particles escape on hyperbolic trajectories (Movie 1).

Images of the particle source locations on Bennu (Fig. 3, A to C) show no obvious geological distinction from other locations on the surface of Bennu. The event radiant locations contain abundant rocks that are diverse in size and surface texture, as well as small circular depressions that may be impact craters. However, similar features are globally distributed on Bennu (*17*, *18*). We analyzed the normal albedo distribution of the two better-constrained source regions (19 January and 11 February) and found that they are similar to the global distribution for Bennu (*19*), averaging 0.042 ± 0.003 (1σ) (Fig. 3, D and E) (*12*). The lack of obvious morphologic or albedo variation may be due to the very low energies associated with the ejection events (discussed below; see Table 1 and table S3).

Characterization of gravitationally bound particles

In addition to particles released in ejection events, we observe a gravitationally bound background population of particles in the Bennu environment (see Fig. 2). Among these are a few objects that remain in orbit for several days, in one case for more than 4.5 days. From among the 215 tracks (linkages of individual detections of the same particle over a short time), we identified a representative group of six distinct gravitationally bound particles for further analysis. Figure 4 shows the trajectories around Bennu of these six particles and their altitude histories. Orbital elements are given in table S4 and fig. S7. Particles 1 to 4 are on short-lived orbits, persisting for 4 to 17 revolutions with lifetimes ranging from 2 to 6 days. These orbits

show a range of inclinations, from near-equatorial to polar. Both prograde and retrograde orbits occur. The semi-major axis of particle 1 is more than 1 km, compared with 0.4 to 0.5 km for particles 2 to 4. Particles 5 and 6 are suborbital. By extrapolating the orbits back to the time when they intersect Bennu's surface, we determine that three of the six particles ejected from the night side of Bennu (between 18:00 and 06:00 LST; table S5). The six particles were ejected with orbital velocities in the range of 15 to 20 cm s^{-1}. Surface-relative velocities at ejection range from roughly 10 to 25 cm s^{-1}.

Particle properties

We constrain the area-to-mass ratios (where area is cross-sectional) of the six bound particles by using the trajectory information and modeling the nongravitational forces, which primarily arise from radiation pressures (table S5) (*12*). The particle trajectories also enable us to calculate the phase angle and range of each observation to the spacecraft, from which we determined the photometric phase functions for particles 1 to 3, thereby constraining the visible absolute magnitude of each particle (table S5). Combining the area-to-mass ratio and absolute magnitude information, and assuming a spherical shape, defines a distinct curve in density (ρ)–albedo (p_V) space for each particle (fig. S8). If we further assume particles with densities of 2 g/cm^3 [based on Bennu meteorite analogs (*20*)], then their normal albedos range from 0.05 to 0.3. In that case, the derived albedos are brighter than 96% of the material on Bennu, and the particle diameters range from 0.4 to 4.4 cm. If, on the other hand, the particles have normal albedos of 0.04, consistent with the average surface material on Bennu (*19*), then the densities range from 0.7 ± 0.3 (1σ) to 1.7 ± 0.4 (1σ) g/cm^3 (fig. S8). The high end of this range is consistent with meteorite

analogs. The lower densities lead to larger particle diameters, ranging from 1.2 to 8.5 cm. Given these uncertainties, we conclude that the particle diameters are in the range <1 to 10 cm.

With these constraints on the particle sizes, and the ejection velocities from the OD analysis, we can estimate the energy of the ejection events (Table 1 and table S3) (*12*). Such estimates should be considered lower limits because we may not have observed all ejected particles. In addition, our calculation assumes that the ejected particles had the average surface albedo of Bennu (0.044; table S3) and the meteorite analog density of 2 g/cm^3. For 6 January, the 124 particles with measured photometry ranged in size from <1 to 8 cm, yielding a minimum event energy of ~270 mJ. For the 19 January event, more than 93 photometrically measured particles with radii between <1 and 7 cm ejected from the surface, giving a minimum event energy of 100 mJ. For 11 February, more than 60 particles with radii between <1 and 7 cm ejected from the surface, with an associated minimum event energy of 8 mJ (see Table 1 for uncertainties on the event energies).

Possible ejection mechanisms

Several constraints apply to the particle ejection mechanism: The three largest observed ejection events occurred in the late afternoon, between 15:22 and 18:05 LST. The largest observed event (6 January) occurred days before Bennu reached perihelion (Fig. 1). The particles left the surface at discrete times. The observed particles range in size from <1 to about 10 cm. The ejection locations occurred over a range of latitudes from 75˚S to 20˚N. Particle velocities range from 0.07 to at least 3.3 m s^{-1}. The minimum kinetic energy of the ejected particles ranges from 8 mJ to 270 mJ, assuming that the particles have albedos equivalent to the surface average of Bennu.

Smaller events occur that eject fewer than 20 observed particles. Individual particles are ejected at a range of local solar times, including at night.

Dust ejection is a common phenomenon in comets and active asteroids. Even for well-studied comets such as 67P/Churyumov-Gerasimenko, substantial uncertainty exists as to the physical mechanism through which particles are released from the surface (*21*). We consider multiple hypotheses for the particle ejection mechanism, evaluating their respective strengths and weaknesses. These include rotational disruption, electrostatic lofting, comet-like ice sublimation, phyllosilicate dehydration, thermally driven stress fracturing, meteoroid impacts, and secondary impacts.

Rotational disruption

Mass shedding or splitting resulting from rotational instability has been identified as a possible explanation for the activity of the smaller active asteroids (*22*). In this scenario, rapidly rotating asteroids experience centrifugal forces greater than the centripetal forces from self-gravity, leading to particle ejection preferentially from low latitudes. Particles launched from Bennu's surface would have a maximum velocity equal to the equatorial surface velocity of 10 cm s^{-1} (based on Bennu's ~250-m equatorial radius and ~4.3-hour rotation period). This mechanism would preferentially produce particles in equatorial orbits in the rotational direction. It is not capable of launching particles on retrograde or hyperbolic trajectories, as we observe.

Electrostatic lofting

Electrostatic lofting is the phenomenon of dust particles detaching from a surface once the electrostatic force on the particles exceeds those of gravity and cohesion (which bind the particles to the surface). The surface of an airless body (e.g., the Moon or an asteroid) interacts directly with the solar wind plasma, which charges the particles and produces a near-surface electric field. The electrostatic force is the product of the grain charge and the local electric field. While electrostatic lofting has been discussed as a possible mechanism of the lunar horizon glow (*23*), when considering cohesion, there remained a discrepancy between the electrostatic force necessary to loft particles and the charging conditions hypothesized to be present in situ (*24*). Charge exchange between individual particles may produce very strong, short-scale electric fields that are capable of lofting particles in microgravity environments (*25*, *26*). It is possible to electrostatically loft particles up to millimeters in radius at small asteroids such as Bennu (*27*), smaller than those we observed. The velocities of electrostatically lofted particles are likely to be less than 1 m s^{-1}, unless additionally accelerated away from the surface by solar radiation pressure (*27*).

Ice sublimation

Dust release from comets is a major source of interplanetary dust particles. On comets, ice sublimation results in gas drag forces that eject dust particles from the surface (*21*). The gas-drag forces accelerate the released dust within a few times the radius of the nucleus, until solar radiation pressure takes over. For such sublimation to be the driver of the Bennu events, ice must be present at or near the surface. Several observed ejection events occurred at relatively low latitudes where temperatures reach ~390 K (*17*). At these temperatures, major cometary ice species (CO, CO_2, and H_2O) are not stable [e.g., (*28*)]. Additionally, there are no water-ice

absorption features at 1.5 or 2.0 μm in spectra of the surface (*20*). Sub-surface ice could be trapped at depths greater than 1 m at some locations for long periods (*29*). Rapid volatile release from such a reservoir would require exposure by large impacts or deep thermal cracking at meter scales. We observe no geologic evidence of such processes acting recently at the event locations (Fig. 3). There is also no evidence of a coma or jets associated with volatile release (Fig. 1 and figs. S3 and S4).

Phyllosilicate dehydration

Although ice has not been observed on Bennu, the surface is rich in water-bearing minerals. Spectroscopy has shown that the surface is dominated by hydrated phyllosilicates, with the closest spectral match being CM-type carbonaceous chondrite meteorites (*20*). Evolved gas analysis experiments on Murchison (a CM chondrite) have demonstrated that considerable volatile release can occur when heated from ambient temperature up to 473 K under vacuum [e.g., *30–32*)]. Although this temperature is ~70 K higher than the peak temperatures on Bennu, such low-temperature water release from Murchison indicates that the thermal dehydration of minerals begins with the loss of weakly bound adsorbed and interlayer water.

Mechanical stresses on Bennu's surface may generate adsorbed water, such as that released in laboratory experiments. The CM chondrites are dominated by Mg-rich serpentine and cronstedtite, an Fe-rich phyllosilicate [e.g., (*33*)]. In these hydrated phases, particle size reduction by grinding enhances dehydroxylation and yields highly disordered material (*34*). The dehydroxylation reaction is substantially accelerated owing to the transformation of structural hydroxyls into adsorbed water in the resulting matrix. If mechanical stresses on Bennu result in a

similar chemical transformation, the structural OH component of the phyllosilicates that dominate the surface mineralogy may be converted into absorbed water concentrated within an outer layer of the surface rocks. It is possible that the release of this adsorbed water within cracks and pores in boulders could provide a gas pressure leading to disruption of rock faces, as thought to occur on near-Earth asteroid (3200) Phaethon (*35*).

Meteoroid impacts

Solid bodies in space are routinely impacted by a steady flux of small meteoroids. Because Bennu is on an Earth-like orbit, we expect the flux of meteoroids at Bennu's surface to be similar to that on Earth, once corrected for gravitational focusing. A model of the interplanetary dust flux in near-Earth space has been determined using data from in situ spacecraft measurements and lunar microcrater studies (*36*), and is widely adopted for meteoroid flux in near-Earth space (*37*). Lunar meteoroids typically impact at velocities between 13 and 18 km s^{-1} (*38*). If we assume an average velocity of 15.5 km s^{-1} for meteoroids at Bennu, an impact by an interplanetary dust particle with mass 2.5 μg would deposit 300 mJ of energy into the surface, consistent with the estimated energy of the largest observed event (6 January). However, Bennu has a cross-sectional area of 1.96×10^5 m^2; applying this value to the interplanetary dust flux model (*36*), we find that Bennu should be hit by a particle of this size on average once every minute, much more frequently than the observed ejection cadence. The large ejection events occurred on a roughly two-week cadence. At that frequency, Bennu should be hit by an average of one meteoroid with a mass ~3000 μg, depositing more than 395,000 mJ of energy into the surface if it impacted at 15.5 km s^{-1}. Thus, only 0.07% of the impact energy from such events would need to be transferred to the particles to produce the largest observed ejection event.

The result of hypervelocity impacts into Bennu's surface depends substantially on the mass and velocity of the impacting grain and on the strength of the target material. Particle impacts at velocities of order 2.5 to 3 km s^{-1} produce well-developed craters with rims, fracturing, and spallation of large number of particles (*39*). At higher speeds, such impact events produce little ejecta; instead, they deposit energy into a small volume of the asteroid surface, causing melting, vaporization, and, at the highest energy densities, ionization of the target and impactor material producing plasma (*40, 41*). It is possible that the observed ejection events are the result of low-velocity meteoroid impacts, which occur much less frequently. Alternatively, the particles may be accelerated by the small fraction of impact energy from more frequent, high-velocity impacts that did not result in plasma production.

Thermal stress fracturing

Bennu's surface experiences extreme temperature variations over its 4.3-hour rotation period. Laboratory studies (*42*) showed that the CM chondrite Murchison quickly developed cracks and spalled particles from diurnal temperature cycling under near-Earth asteroid surface conditions. At the mid-latitudes, where the 19 January and 11 February events occurred, the surface temperature plunges to 250 K in the pre-dawn hours and reaches a peak of 400 K at ~13:00 LST (*12*). Because Bennu has a moderate thermal inertia of 350 J m^{-2} K^{-1} $s^{-½}$ (*17*), the maximum temperature at the thermal skin depth (penetration depth of daily thermal conduction) of ~2 cm occurs later in the afternoon, at ~16:00 LST. The amplitude of temperature variation falls by a factor of *e* at one thermal skin depth. Thus, for a region on Bennu whose maximum surface

temperature is 400 K, the peak temperature at a depth of ~2 cm reaches 325 K, inducing a strong thermal gradient over this short distance that cycles every 4.3 hours.

Thermal cycling can drive the growth of cracks in rocks over a range of spatial scales within the thermal skin depth, controlled by the amplitude and frequency of the temperature cycle, mineral composition, constituent grain size, the overall rock shape, and its orientation relative to the Sun. At the bulk scale, stresses associated with temperature gradients and surface cooling are induced in different regions of a boulder at different times throughout the thermal cycle. Stresses arising in the shallow interior of large boulders tend to drive surface-parallel crack propagation (*43*). In the thermal fatigue regime, subcritical crack growth occurs slowly, propagating fractures incrementally over many cycles. Crack propagation velocity increases with crack length, until catastrophic disruption occurs, which may disaggregate material and eject particles from the surface.

In terrestrial settings, thermal fatigue combined with tectonic unloading is known to cause rock dome exfoliation and energetic particle ejection (*44*). In these studies, rocks show the greatest evidence for stress and microfracturing in the afternoon and evening. Although the tectonic unloading effects, which are not likely to be present on Bennu, are thought to add to the energy in these events, much less energy is needed to eject particles in a microgravity environment. Such energy may be stored as a result of structural deformation related to thermal strain, providing excess energy leading to particle ejection (*35*).

Secondary surface impacts

A possible mechanism for the small ejection events is the re-impact of disaggregated material released by larger events. Analysis of particle trajectories in the largest events show that the particles have a substantial velocity component in the direction of asteroid rotation. Because the largest events occur in the afternoon, a large fraction of the particles on suborbital trajectories impact the night side of the asteroid (Movie 1). During impact, these particles may bounce off the surface or collide with other small particles on the surface, resulting in subsequent ejection of a small number of low-velocity particles.

Dynamical calculations show that ejecta moving at surface-relative velocities up to 30 cm s^{-1} (escape velocity of ~20 cm s^{-1} plus Bennu's surface rotational velocity of 10 cm s^{-1}) lofted from the surface of Bennu can re-impact the surface days later (Movie 1). Depending on the impact location, re-impacting particles may be re-launched into a sub-orbital trajectory by bouncing off a hard surface such as a boulder (*45*) or ricocheting off a fine-grained surface (*46*, *47*). Numerical simulations show that impacts on a fine-grained surface may result in the ejection of smaller surface particles at launch speeds that exceed the escape speed of Bennu (fig. S9). However, we have not directly observed particles ejecting from Bennu that are as large as the impactors in these simulations; in the energy regime that we have observed, particles of that size would not have traveled far enough from the asteroid to be detectable in our images. Our assessment thus leaves three viable candidates for the primary ejection mechanism: phyllosilicate dehydration, meteoroid impacts, and thermal stress fracturing (see Conclusions).

Evidence from Bennu's geology

Particle ejection from rock surfaces is consistent with the widespread observation of exfoliation features on Bennu's surface (Fig. 5 and fig. S10). Exfoliation is the division of a rock mass into lenses, plates, or parallel "sheets" due to differential stresses (*48*). For some bright boulders on Bennu (e.g., Fig. 5A), lineation is present on the rock faces, and they exhibit sheets that parallel the direction of fracture propagation. The more abundant dark boulders on Bennu also exhibit exfoliation (e.g., Fig. 5C). In these rocks, the exfoliation fractures are linear, but the finer-grained texture appears as blocky segments in the fracture profile. Spalled fragments are seen resting on the surface and lying around the base of dark boulders.

The observed textures are characteristic of surface stresses that drive surface-perpendicular cracking, segment exfoliation sheets, and cause near-surface disaggregation. We do not observe similar spalled fragments in the immediate vicinity of the brighter boulders. However, we observe bright rocks perched on the surfaces of boulders, in orientations that exhibit no evident alignment with the underlying boulder's texture (for example, the bright object in the center-right of Fig. 5C). These bright rocks tend to have plate-like morphologies, similar to the exfoliation textures observed on the flat surfaces of the brighter rocks. Thus, exfoliation and fracturing may be operating on all boulders on Bennu, but the response of the bright rocks may be different—ejecting material over large distances, even on hyperbolic escaping trajectories, whereas the darker boulders decompose on site, creating a halo of spalled fragments.

Implications for Bennu's geophysics

The existence of low-energy particle ejection events on Bennu may result in re-impacting particles preferentially concentrated within the boundaries of Bennu's rotational Roche lobe (the region where material is energetically bound to the asteroid surface, between latitudes of ~±23°) (*16*). A random distribution of ejection events with a sizable fraction of particle velocities less than the escape speed will preferentially transport material toward the equator owing to the lower geopotential. Once within the Roche lobe, the particles are trapped inside unless given a large enough speed (a few centimeters per second) and will be redistributed within the lobe owing to the chaotic orbital environment whenever lofted (*16*). Particles ejected with higher energies that achieve orbit will preferentially re-impact in the equatorial region within the lobe because of the larger asteroid radius there [(*16*), their figure 5]. After impact (which occurs at low speeds relative to the escape velocity), the particles will not have sufficient energy to escape the Roche lobe and again will be preferentially trapped, leading to a concentration of returning particles in these regions, as opposed to a globally uniform distribution.

Previous observations have indicated a steady increase in Bennu's rotation rate that will lead to doubling of that rate in about 1.5 million years; this acceleration is consistent with the Yarkovsky–O'Keefe–Radzievskii–Paddack (YORP) effect (*10*, *49*). The angular momentum associated with particles ejected on escaping trajectories could also influence the rotation rate. It is possible to generate the measured rotational acceleration of Bennu by ejecting several particles of diameter ~10 cm once per day in the westward direction from the equator, assuming no concurrent water vapor loss. A random ejection of escaping particles from the surface of a spinning body would produce a spin deceleration (*50*).

We summed the net angular momentum change from particles launched normal to every facet on the asteroid surface and given a sufficient ejection speed for escape (*12*, *16*). We found that such a flux would always cause Bennu to spin slower (fig. S11), counteracting the YORP effect (*50*). This implies that the strength of the YORP effect on Bennu due to solar photons could be greater than originally estimated (*10*, *49*). If Bennu were to eject, for example, on the order of twenty 10-cm particles per day at a speed of 18 cm s^{-1} (the speed at which the effect is the greatest) normal to random points on its surface, then on average, its rotational acceleration would be slowed by less than 1% of the measured rotational acceleration. Thus, when averaged over the entire surface, the net effect of particle ejection is negligible relative to the YORP effect.

The linear momentum transfer from the particle ejections is orders of magnitude lower than that of the transverse acceleration due to thermal emission from Bennu, the operative component for the Yarkovsky effect (*51*). This acceleration peaks at ~10^{-12} m s^{-2} during perihelion (*51*). Such an acceleration leads to a daily change in velocity ΔV of 10^{-7} m s^{-1}, which is more than 7000 times the ΔV caused by a single 10-cm particle with a density of 2 g/cm^3 escaping at 1 m s^{-1}.

Conclusions and broader implications

The ejection events on Bennu inform our understanding of active asteroids. There are substantial differences between active asteroids as commonly defined—where major mass loss events occur via processes such as large impacts, volatile release, and rotational acceleration leading to mass shedding—and relatively small mass loss events as we see on Bennu. It is likely that there is a

continuum of event magnitudes, and that we have been limited to observing only the largest phenomena.

Mass loss observed during perihelion from the B-type near-Earth asteroid (3200) Phaethon, the parent body of the Geminids meteor shower, apparently consists of smaller particles [1 μm (*52*)] than observed at Bennu (~1 to ~10 cm). However, particles in the centimeter size range were not observable during studies of Phaethon at perihelion and sub-cm particles would have been difficult to detect in NavCam 1 images. Particles in the millimeter size range are observed as Geminids meteors (*53*). The mass loss from Bennu between 31 December and 18 February (including the three largest ejection events characterized above) was ~10^3 g, which is orders of magnitude less than Phaethon's near-perihelion mass loss (~10^4 to 10^5 kg per perihelion passage) (*7*). The mass loss rate (~10^{-4} g s^{-1}) on Bennu is also many orders of magnitude less than the rates observed at other active asteroids (~10 to 10^3 g s^{-1}) (*1*). Mass loss as seen at Bennu suggests that Phaethon's current mass loss rate may include larger particles and be greater than remote observations imply.

Having evaluated multiple hypotheses for the mechanism of particle ejection on Bennu, we find that thermal fracturing, volatile release by dehydration of phyllosilicate rocks, and meteoroid impacts are plausible explanations. Rotational disruption and electrostatic lofting cannot explain the observed particle sizes and ejection velocities. There is no evidence for ice on the surface of Bennu or for recent exposure of a sub-surface ice reservoir at the multiple ejection sites. Bennu's boulder morphology and the event ejection times are consistent with exfoliation resulting from thermal fracturing, phyllosilicate dehydration, or an interplay between these two mechanisms.

Because we expect meteoroid flux to be greatest in the leading hemisphere (late afternoon on Bennu due to its retrograde rotation), the ejection event times are also consistent with meteoroid impacts. It is possible that multiple mechanisms operate in combination. Re-impacting particles could play a role in the smaller ejections or contribute to the larger events.

The particles that escape from Bennu on parabolic or hyperbolic orbits will escape onto heliocentric orbits, which we expect to disperse over time into a meteoroid stream. Based on the measured ejection velocities, meteoroids released after 1500 CE would not have spread wide enough to bridge the current distance between the orbits of Bennu and Earth, 0.0029 au, but will do so when that distance decreases later in the 21st century (*54*). However, if Bennu was active in the past, and the ejected particles survive for thousands of years, planetary perturbations would spread the stream wide enough to cause an annual meteor shower on present-day Earth around 23 September. The shower would radiate from a geocentric radiant at right ascension 5º, declination –34º, and speed 6.0 km s^{-1} (*54*), corresponding to an apparent entry speed of 12.7 km s^{-1} (*12*). Meteoroids moving this slowly would create meteors of integrated visual magnitude +2 to –5, assuming an 0.7% luminous efficiency (*55*). The stream would not easily blend with the sporadic background over thousands of years. No shower is detected in current meteor orbit survey data (*56*), but those data have poor coverage in the Southern Hemisphere.

The primary objective of OSIRIS-REx is to return samples of centimeter-scale rocks from the surface of Bennu to Earth for analysis (*14*). We have observed centimeter-scale particles frequently being ejected and re-impacting the asteroid surface. It is possible that the collected sample will contain some particles that were ejected and returned to Bennu's surface.

References

1. D. Jewitt, H. Hsieh, J. Agarwal. “The active asteroids”, in *Asteroids IV*, P. Michel, F. E. DeMeo, W. F. Bottke, eds. (Univ. of Arizona Press, 2015), pp. 221–241.

2. E.W. Elst, G. Pizarro, et al. Comet P/1996 N2 (ELST-PIZARRO). IAU Circular 6456 (1996).

3. D. Jewitt et al. Hubble Space Telescope Investigation of Main-belt Comet 133P/Elst-Pizarro. *Astronomical Journal* **147**, 117 (2014).

4. D. Jewitt et al. Episodically Active Asteroid 6478 Gault. *Astrophysical Journal Letters* **876**, L19 (2019).

5. F. Moreno, J. Licandro, A. Cabrera-Lavers, F.J. Pozuelos, Early evolution of disrupted asteroid P/2016 G1 (PANSTARRS). *Astrophysical Journal Letters* **826**, L22 (2016).

6. J. Li, D. Jewitt, Recurrent Perihelion Activity in (3200) Phaethon. *Astronomical Journal* **145**, 154 (2013).

7. M.-T. Hui, J. Li, Resurrection of (3200) Phaethon in 2016. *Astronomical Journal* **153**, 23 (2017).

8. D. Jewitt, The active asteroids. *Astronomical Journal* **143**, 66 (2012).

9. Lauretta, D.S. et al. The OSIRIS-REx target asteroid (101955) Bennu: Constraints on its physical, geological, and dynamical nature from astronomical observations. *Meteorit. Planet. Sci.* **50**, 834–849 (2015).

10. C.W. Hergenrother et al. The operational environment and rotational acceleration of asteroid (101955) Bennu from OSIRIS-REx observations. *Nature Communications* **10**, 1291 (2019).

11. M.G. Daly, O.S. Barnouin, C. Dickinson, J. Seabrook, C.L. Johnson, G. Cunningham, T. Haltigin, D. Gaudreau, C. Brunet, I. Aslam, A. Taylor, E.B. Bierhaus, W. Boynton, M. Nolan, D.S. Lauretta, The OSIRIS-REx Laser Altimeter (OLA) investigation and instrument. *Space Science Reviews* **212**, 899–924 (2017).

12. Materials and methods are available as supplementary materials.

13. B.J. Bos et al. Touch And Go Camera System (TAGCAMS) for the OSIRIS-REx asteroid sample return mission. *Space Science Reviews* **214**, 37 (2018).

14. D. S. Lauretta et al., OSIRIS-REx: Sample Return from Asteroid (101955) Bennu. *Space Science Reviews* **212**, 925–984 (2017).

15. B. Williams et al., OSIRIS-REx Flight Dynamics and Navigation Design. *Space Science Reviews* **214**, 69 (2018).

16. D. J. Scheeres et al., The dynamic geophysical environment of (101955) Bennu based on OSIRIS-REx measurements. *Nature Astronomy* **3**, 352–361 (2019).

17. D. N. DellaGiustina et al., Properties of rubble-pile asteroid (101955) Bennu from OSIRIS-REx imaging and thermal analysis. *Nature Astronomy* **3**, 341–351 (2019).

18. K. J. Walsh et al., Craters, boulders and regolith of (101955) Bennu indicative of an old and dynamic surface. *Nature Geoscience* **12**, 242–246 (2019).

19. D.S. Lauretta et al., The unexpected surface of asteroid (101955) Bennu. *Nature* **568**, 55–60 (2019).

20. V. E. Hamilton et al., Evidence for widespread hydrated minerals on asteroid (101955) Bennu. *Nature Astronomy* **3**, 332-340 (2019).

21. J.-B. Vincent et al., Local manifestations of cometary activity. *Space Science Reviews* **215**, 30 (2019).

22. M. Drahus et al., Fast rotation and trailing fragments of the active asteroid P/2012 F5 (Gibbs). *The Astrophysical Journal Letters* **802**, L8 (2015).

23. J. J. Rennilson, D.R. Criswell, Surveyor Observations of Lunar Horizon-Glow. *The Moon* **10**, 121–142 (1974).

24. C. M. Hartzell, D. J. Scheeres, The Role of Cohesive Forces in Particle Launching on the Moon and Asteroids. *Planetary and Space Science* **59**, 1758–1768 (2014).

25. X. Wang et al., Dust Charging and Transport on Airless Planetary Bodies. *Geophysical Research Letters* **43**, 6103–6110 (2016).

26. M. I. Zimmerman et al., Grain-Scale Supercharging and Breakdown on Airless Regolith. *Journal of Geophysical Research: Planets* **121**, 2016JE005049 (2016).

27. C. M. Hartzell, Dynamics of 2D electrostatic dust levitation at asteroids. *Icarus* 333, 234–242 (2019).

28. E. L. Andreas, New estimates for the sublimation rate of ice on the Moon. *Icarus* **186**, 24–30 (2007).

29. N. Schorghofer, Predictions of depth-to-ice on asteroids based on an asynchronous model of temperature, impact stirring, and ice loss. *Icarus* **276**, 88–95 (2016).

30. E.K. Gibson, Jr., Inorganic gas release studies and thermal analysis investigations on carbonaceous chondrites. *Meteoritics* **9**, 343–344 (1974).

31. I. L. ten Kate et al., VAPoR – Volatile Analysis by Pyrolysis of Regolith – an instrument for in situ detection of water, noble gases and organics on the Moon. *Planet. Space Sci.* **58**, 1007–1017 (2010).

32. E. K. Gibson, Jr., S. M. Johnson, Thermogravimetric-quadrupole mass-spectrometric analysis of geochemical samples. *Thermochimica Acta* **4**, 49–56 (1972).

33. D. S. Lauretta, X. Hua, P. R. Buseck, Mineralogy of fine-grained rims in the ALH 81002 CM chondrite. *Geochimica et Cosmochimica Acta* **64**, 3263–3273 (2000).

34. A. Drief, F. Nieto, The effect of dry grinding on antigorite from Mulhacen, Spain. *Clays and Clay Minerals* 47, 417–424 (1999).

35. D. Jewitt, J. Li, Activity in geminid parent (3200) Phaethon. *The Astronomical Journal* **140**, 1519 (2010).

36. E. Grün, H.A. Zook, H. Fechtig, R.H. Giese, Collisional balance of the meteoritic complex. *Icarus* **62**, 244–272 (1985).

37. Committee for the Assessment of NASA's Orbital Debris Programs, Aeronautics and Space Engineering Board, Division on Engineering and Physical Sciences, *Limiting Future Collision*

Risk to Spacecraft: An Assessment of Nasa's Meteoroid and Orbital Debris Programs (National Research Council, 2011).

38. H. A. Zook, "The state of meteoritic material on the Moon," in *Lunar Science VI*, 1301 (1975).

39. K. Fiege et al., Space Weathering Induced Via Microparticle Impacts: 2. Dust Impact Simulation and Meteorite Target Analysis. *Journal of Geophysical Research: Planets* **124**, 1084–1099 (2019).

40. M. S. Thompson et al., Microchemical and structural evidence for space weathering in soils from asteroid Itokawa. *Earth, Planets and Space* 66, 89 (2014).

41. S. Drapatz, K. W. Michel, Theory of shock-wave ionization upon high-velocity impact of micrometeorites. *Zeitschrift für Naturforschung A* **29**, 870–879 (1974).

42. M. Delbo et al., Thermal fatigue as the origin of regolith on small asteroids. *Nature* **508**, 233 (2014).

43. J. L. Molaro, S. Byrne, J.-L. Le, Thermally induced stresses in boulders on airless body surfaces, and implications for rock breakdown. *Icarus* **294**, 247–261 (2017).

44. B. D. Collins et al., Thermal influences on spontaneous rock dome exfoliation. *Nature Communications* **9**, 762 (2018).

45. H. Yano et al., Touchdown of the Hayabusa spacecraft at the Muses Sea on Itokawa. *Science* **312**, 1350–1353 (2006).

46. C. Maurel et al., Numerical simulations of the contact between the lander MASCOT and a regolith-covered surface. *Advances in Space Research* **62**, 2099–2124 (2018).

47. F. Thuillet, P. Michel, C. Maurel, R.-L. Ballouz, Y. Zhang, D.C. Richardson, J. Biele, E. Tastumi, S. Sugita, Numerical modeling of lander interaction with a low-gravity asteroid regolith surface: Application to MASCOT onboard Hayabusa2. *Astron. Astrophys.* **615**, A41 (2018).

48. G. R. Holzhausen, Origin of sheet structure, 1. Morphology and boundary conditions. *Eng. Geol.* **27**, 225–278 (1989).

49. M. C. Nolan et al., Detection of rotational acceleration of Bennu using HST lightcurve observations. *Geophysical Research Letters* **46**, 1956–1962, (2019).

50. A.R. Dobrovolskis, J.A. Burns, Angular momentum drain: a mechanism for despinning asteroids. *Icarus* **57**, 464–476 (1984).

51. S. R. Chesley et al., Orbit and bulk density of the OSIRIS-REx target Asteroid (101955) Bennu. *Icarus* **235**, 5–22 (2014).

52. D. Jewitt, J. Li, J. Agarwal, The dust tail of asteroid (3200) Phaethon. *Astrophysical Journal Letters* **771**, L36 (2013).

53. V. Vojáček et al., Properties of small meteoroids studied by meteor video observations. *Astronomy & Astrophysics* **621**, A68 (2019).

54. Q. Ye, Prediction of meteor activities from (101955) Bennu. *Research Notes of the AAS* **3**, 56 (2019).

55. R. J. Weryk, P. G. Brown, Simultaneous radar and video meteors – II: Photometry and ionisation. *Planetary and Space Science* **81**, 32–47 (2013).

56. P. Jenniskens, P. S. Gural, L. Dynneson, B. J. Grigsby, K. E. Newman, M. Borden, M. Koop, D. Holman, CAMS: Cameras for Allsky Meteor Surveillance to establish minor meteor showers. *Icarus* **216**, 40–61 (2011).

57. A. J. Liounis, J. L. Small, J. C. Swenson, J. R. Lyzhoft, B.W. Ashman, K. M. Getzandanner, M. C. Moreau, C. D. Adam, J. M. Leonard, D. S. Nelson, J. Y. Pelgrift, B. J. Bos, S. R. Chesley, C. W. Hergenrother, D. S. Lauretta, Autonomous detection of particles and tracks in optical images. arXiv (2019).

58. D. Tody, “The IRAF Data Reduction and Analysis System,” in *Instrumentation in Astronomy VI*, ed. D.L. Crawford, *Proc. SPIE* **627**, 733 (1986).

59. N. H. Samarasinha, S. M. Larson, Image enhancement techniques for quantitative investigations of morphological features in cometary comae: a comparative study. *Icarus* **239**, 168–185 (2014).

60. C. D. Jackman, P. J. Dumont, “Optical navigation capabilities for deep space missions,” in *Spaceflight Mechanics 2013*, S. Tanygin et al., eds. (Univelt, 2013), pp. 3191–3209.

61. C. D. Jackman, D. S. Nelson, L. K. McCarthy, T. J. Finley, A. J. Liounis, K. M. Getzandanner, P. G. Antreasian, M. C. Moreau, “Optical navigation concept of operations for the OSIRIS-REx Mission,” in *Spaceflight Mechanics 2017*, J. W. McMahon et al., eds. (Univelt, 2017), pp. 3337–3354.

62. W. A. Joye, E. Mandel, “New features of SAOImage DS9,” in *Astronomical Data Analysis Software and Systems XII*, H. E. Payne, R. I. Jedrzejewski, R. N. Hook, eds. (ASP Conference Series, vol. 295, Astronomical Society of the Pacific, 2003), pp. 489–492.

63. C. Acton, N. Bachman, B. Semenov, E. Wright, SPICE tools supporting planetary remote sensing. *International Archives of the Photogrammetry, Remote Sensing and Spatial Information Sciences* **41**, 357–359 (2016).

64. O. S. Barnouin et al., Shape of (101955) Bennu indicative of a rubble pile with internal stiffness. *Nature Geoscience* **12**, 247–252 (2019).

65. M. Matsumoto, T. Nishimura. Mersenne twister: A 623-dimensionally equidistributed uniform pseudo-random number generator. *ACM Transactions on Modeling and Computer Simulation* **8**, 3–30 (1998).

66. J. R. Quinn, P. Wolff, "TOPEX/Poseidon operational orbit determination results using global positioning satellites," in *Astrodynamics 2013*, A. K. Misra et al., Eds. (Univelt, 1993), pp. 143–158.

67. T.D. Moyer, *Formulation for Observed and Computed Values of Deep Space Network Data Types for Navigation* (Wiley, 2003).

68. Jet Propulsion Laboratory, MONTE: Mission Analysis, Operations, and Navigation Toolkit Environment (2019); https://montepy.jpl.nasa.gov/.

69. R. B. Blackman. Methods of orbit refinement. *Bell System Technical Journal* **43**, 885–909 (1964).

70. A. Milani et al., The asteroid identification problem: III. Proposing identifications. *Icarus* **144**, 39-53 (2000).

71. A. Milani, M. E. Sansaturio, S. R. Chesley, The asteroid identification problem IV: Attributions. *Icarus* **151**, 150–159 (2001).

72. M. Brozović, A. Jacobson, The orbits of Jupiter's irregular satellites. *Astron. J.* **153**, 147 (2017).

73. Jet Propulsion Laboratory, NAIF: Navigation and Ancillary Information Facility (2019); https://naif.jpl.nasa.gov/naif/index.html.

74. C. A. Murray, *Vectorial Astrometry* (CRC Press, 1983).

75. G. J. Bierman, *Factorization Methods for Discrete Sequential Estimation* (Academic Press, 1977).

76. R.A. Werner, D.J. Scheeres, Exterior gravitation of a polyhedron derived and compared with harmonic and mascon gravitation representations of asteroid 4769 Castalia. *Celestial Mechanics and Dynamical Astronomy* **65**, 313–344 (1997).

77. Y. Takahashi, D. J. Scheeres, Small body surface gravity fields via spherical harmonic expansions. *Celestial Mechanics and Dynamical Astronomy* **119**, 169–206 (2014).

78. R. A. Werner, The gravitational potential of a homogeneous polyhedron or don't cut corners. *Celestial Mechanics and Dynamical Astronomy* **59**, 253–278 (1994).

79. J. L. Geeraert et al., OSIRIS-REx navigation small force models. Paper AAS 19-717 presented at the AAS/AIAA Astrodynamics Specialists Conference, Portland, ME, 11 to 15 August 2019.

80. B. Rizk et al., OCAMS: The OSIRIS-REx Camera Suite. *Space Sci. Rev.* **214**, 26 (2018).

81. D. N. DellaGiustina et al., Overcoming the challenges associated with image-based mapping of small bodies in preparation for the OSIRIS-REx mission to (101955) Bennu. *Earth and Space Science* **5**, 929–949 (2018).

82. U.S. Geological Survey, ISIS: Integrated Software for Imagers and Spectrometers (2019); https://isis.astrogeology.usgs.gov/.

83. K. Muinonen et al., A three-parameter magnitude phase function for asteroids. *Icarus* **209**, 542–555 (2010).

84. J.W. Fowler, J.R. Chillemi, "IRAS asteroid data processing," in *The IRAS Minor Planet Survey*, E. F. Tedesco, ed. (Tech. Rpt. PL-TR-92-2049, Phillips Laboratory, Hanscom Air Force Base, Massachusetts, 1992), pp. 17–43.

85. D. Brack, J. McMahon, Modeling the coupled dynamics of an asteroid with surface boulder motion. *Icarus* **333**, 96-112 (2019).

86. D.J. Scheeres, *Orbital Motion in Strongly Perturbed Environments: Applications to Asteroid, Comet and Planetary Satellite Orbiters* (Springer-Praxis Books in Astronautical Engineering, 2012).

87. B. Rozitis, S. F. Green, Directional characteristics of thermal–infrared beaming from atmosphereless planetary surfaces–a new thermophysical model. *Monthly Notices of the Royal Astronomical Society* **415**, 2042–2062 (2011).

88. B. Rozitis, S. F. Green, The influence of rough surface thermal-infrared beaming on the Yarkovsky and YORP effects. *Monthly Notices of the Royal Astronomical Society* **423**, 367–388 (2012).

89. B. Rozitis, S. F. Green, The influence of global self-heating on the Yarkovsky and YORP effects. *Monthly Notices of the Royal Astronomical Society* **433**, 603–621 (2013).

90. S. R. Schwartz et al., An implementation of the soft-sphere discrete element method in a high-performance parallel gravity tree-code. *Granular Matter* **14**, 363–380 (2012).

91. R.-L. Ballouz, Numerical Simulations of Granular Physics in the Solar System. Thesis, University of Maryland, College Park, MD, 2017.

92. P. Jenniskens, *Meteor Showers and Their Parent Comets* (Cambridge Univ. Press, 2006).

Acknowledgments: We are grateful to the entire OSIRIS-REx Team for making the encounter with Bennu possible.

Funding: This material is based upon work supported by NASA under Contracts NNM10AA11C and NNG13FC02C issued through the New Frontiers Program. A portion of this work was conducted at the Jet Propulsion Laboratory, California Institute of Technology under a contract with the National Aeronautics and Space Administration. OLA and funding for the Canadian authors was provided by the Canadian Space Agency. C.M.H., J.L.M., and P.T. acknowledge support from NASA's OSIRIS-REx Participating Scientist Program (grants 80NSSC18K0227, 80NSSC18K0239, and 80NSSC18K0280, respectively). P.M., G.L., and F.T. acknowledge funding support from the French Agency CNES and from the Academies of Excellence on Complex Systems and Space, Environment, Risk and Resilience of the Initiative d'EXcellence "Joint, Excellent, and Dynamic Initiative" (IDEX JEDI) of the Université Côte d'Azur. J.L. and J.d.L. acknowledge funding support from the projects AYA2015-67772-R (MINECO, Spain) and ProID20170112 (ACIISI/Gobierno de Canarias/EU/FEDER). B.Ro. acknowledges funding support from the Royal Astronomical Society (RAS) and the UK Science and Technology Facilities Council (STFC).

Author contributions: D.S.L. led the scientific investigation and developed the hypotheses for ejection mechanisms. C.W.H. detected the particle ejection events and led the photometric modeling. C.K.M., J.N.K.Jr., and J.-Y.L. supported the photometric modeling efforts. S.R.C. led

the team that performed the orbital element analysis of the six short-lived orbiting particles, supported by R.A.J., M.B., A.B.D., D.F., Y.T., W.M.O.Jr., D.J.S., and J.W.M. D.J.S. also calculated the Bennu Roche lobe and contribution of particle ejections to Bennu's observed rotational acceleration and Yarkovsky. M.C.M. led the team that performed the OpNav and orbit determination analyses. J.M.L. performed the orbit determination analysis for the three largest observed ejection events. J.Y.P. led the OpNav characterization of the three largest events, supported by A.J.L., E.J.L.-C., C.D.A., D.S.N., L.K.M., and E.M.S. M.G.D. is the lead instrument scientist for OLA and performed the analysis of the off-body lidar returns, supported by M.A.A. and J.A.S. B.J.B. is the lead instrument scientist for NavCam 1 and performed image calibration and image processing for the navigation images. B.Ri. and C.Y.d.'A. are the lead and deputy lead instrument scientists, respectively, for the OSIRIS-REx Camera Suite; they analyzed images of Bennu's surface for evidence of particle infall and processed the images used for the stereo pairs. D.N.D. is the lead image processing scientist for OSIRIS-REx and prepared the global mosaics used to register the particle source locations, supported by K.J.B., C.A.B., and D.R.G. K.J.B. also developed the NavCam camera model for use in registering NavCam images relative to the Bennu shape model and the background star fields. J.P.E. is the lead thermal analysis scientist for OSIRIS-REx, and B.Ro. developed the asteroid thermal model to determine the surface temperatures, skin depths, and thermal gradients at the particle ejection sites and globally across the asteroid. R.-L.B. developed the secondary impact hypothesis with support from P.M. and F.T. W.F.B. provided input on the meteoroid impact hypothesis and evaluated the other hypotheses in the context of the dynamical evolution of Bennu. H.C., J.d.L., and J.L. provided expertise on other known active asteroids. H.C.C.Jr. provided input on the potential mechanisms for ejection events and on the content of the manuscript. J.P.D. provided rock count

data for testing the re-impacting particle hypothesis. D.P.G. counted rocks and provided input on EGA studies of meteorites and their low-temperature volatile release. C.M.H. developed the electrostatic lofting hypothesis. P.J. developed the hypothesis on the potential Bennu meteor shower. E.R.J. performed the geologic analysis of the particle ejection source regions. G.L. provided input on the relevance of thermal cycling experiments and regolith evolution. C.M. and B.M. identified and processed the stereo pair images. J.L.M. provided input on the feasibility of thermal fracture processes as a mechanism for particle ejection. H.L.R. led the development of the figures. S.H.S. provided software for processing NavCam images and identifying candidate particles. P.T. performed calculations for the statistical assessment of particles lifetime and fallback distribution. D.V. supported the development of the force model for nongravitational forces for orbiting particles, as well as giving input on the general implications and context of Bennu's activity. C.W.V.W. contributed substantively to the writing and preparation of the manuscript.

Competing interests: H.C.C.Jr. is also affiliated with the Department of Earth and Planetary Science, American Museum of Natural History, New York, NY, USA. J.L.M. is also affiliated as a contractor with the Jet Propulsion Laboratory, California Institute of Technology, Pasadena, CA, USA.

Data and materials availability: NavCam 1 images from Orbital A and OLA data from Preliminary Survey are available via the Planetary Data System (PDS) (https://sbn.psi.edu/pds/resource/orex/; NavCam 1 data are part of the TAGCAMS bundle). The NavCam 1 images that we used are listed in data S1. The parameters of the three largest ejection

events are given in tables S2 and S3, and the derived orbital data for the six gravitationally bound particles are in tables S4 and S5 and data S1.

Supplementary Materials

[link]

Materials and Methods

Figs. S1 to S11

Tables S1 to S5

References (*57*–*92*)

Data S1

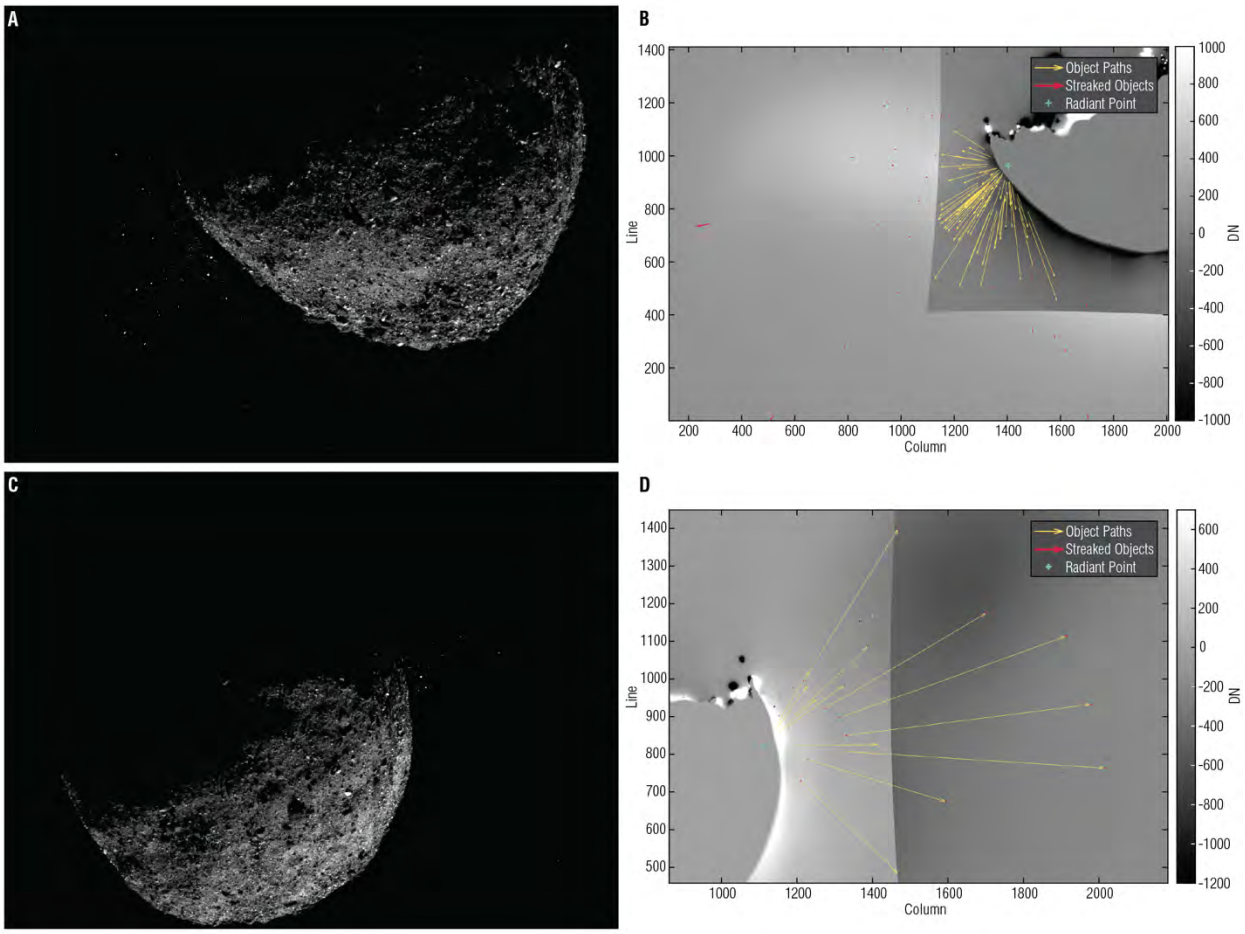

Fig. 1. Particle ejections from Bennu. (**A** and **C**) Composite views of particle ejections from the surface of asteroid Bennu on 6 January (A) and 19 January (C). These images were produced by combining two exposures taken by the NavCam 1 imager in immediate succession: a short-exposure image (1.4 ms), showing the asteroid, and a long-exposure image (5 s), showing the particles (*12*). Image processing techniques were applied to increase the brightness and contrast of the ejected particles, which would otherwise be invisible at the same time as the bright asteroid surface (*12*). The original images are shown in fig. S3. In (A), Bennu's north (+*z*) pole is to the upper right, pointing into the image; the sub-observer latitude is –36°. In (C), the north pole is to the upper right, pointing out of the image; the sub-observer latitude is 60°. (**B** and **D**) In each panel, two NavCam images taken immediately after the ejection events on 6 January (B)

and 19 January (D) are registered on the center of Bennu and differenced to highlight any moving particles. Particles moving at high velocity appear as streaks in a single image (red) that provide position information at the start and end of the exposure. The paths of particles moving more slowly (yellow) are identified from individual particles detected in the first image that also are present in the second image, farther from Bennu's limb. For each event, the apparent motion of the individual particles traces back to a radiant point on Bennu's surface (teal cross) that indicates the potential source region on the near side of Bennu. A second possible source region occurs on the far side of Bennu, out of view. The shaded area closest to the asteroid [darker shading in (B), lighter shading in (D)] corresponds to where the two images share a common field of view and are differenced. The opposite shading corresponds only to the image with the larger field of view [earlier image in (B), later image in (D)]. DN, data number.

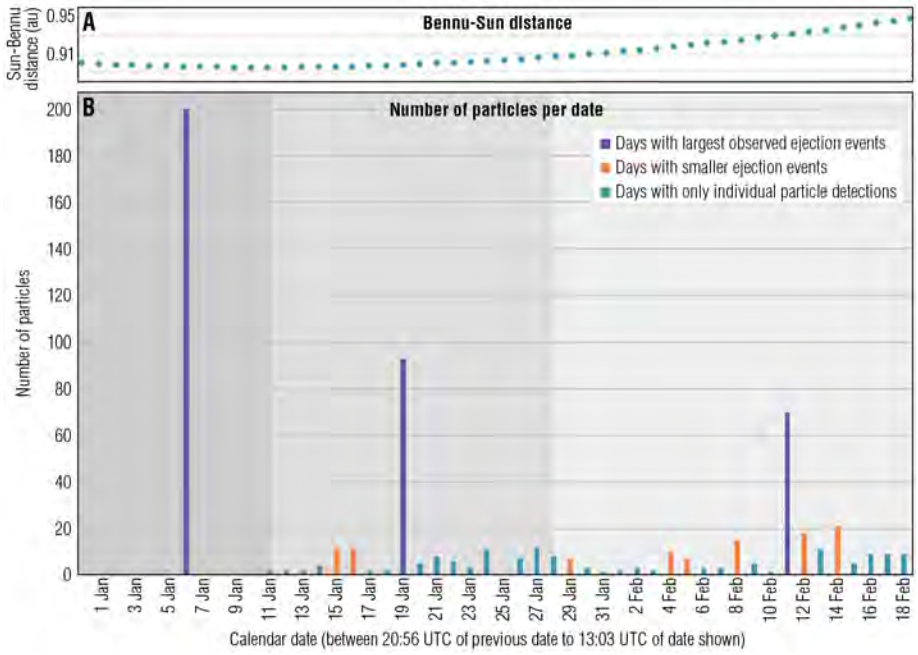

Fig. 2. Particle detections during the Orbital A mission phase. (**A**) Distance of Bennu from the Sun over the same time period as shown in (B). (**B**) Particle detections associated (purple and orange) and not associated (teal) with observed ejection events. The changes in the background shading indicate when the observation cadence increased on 11 January and again on 28 January 2019.

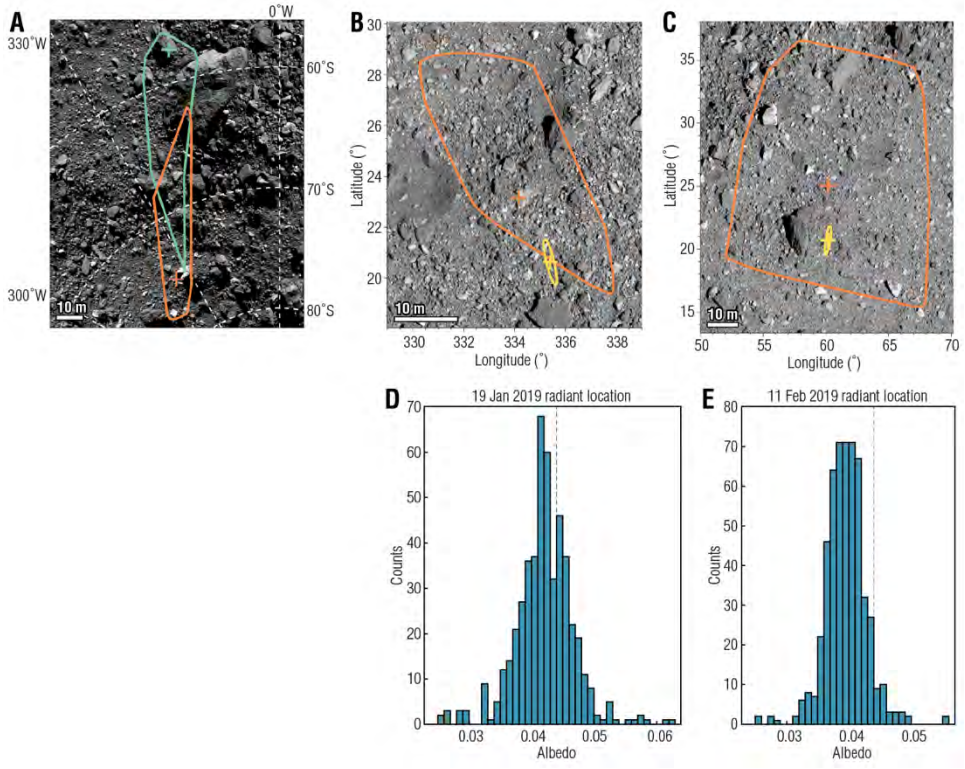

Fig. 3. Ejection source regions and their surface albedo distributions. Radiant locations of the (**A**) 6 January, (**B**) 19 January, and (**C**) 11 February particle ejection events are overlain on a global mosaic of Bennu (*12*). Orange and teal crosses indicate the far and near candidate radiant locations, respectively, determined from OpNav analysis; orange and teal outlines enclose the 3σ uncertainty region. The yellow crosses indicate the most likely source location determined from OD analysis; yellow lines trace the 3σ uncertainty. (**D** and **E**) For the locations of the latter two events, which are more tightly constrained, we show the surface albedo distributions (radiant locations with 3σ uncertainties) (*12*). The dashed vertical lines indicate the average albedo of Bennu's surface (*19*).

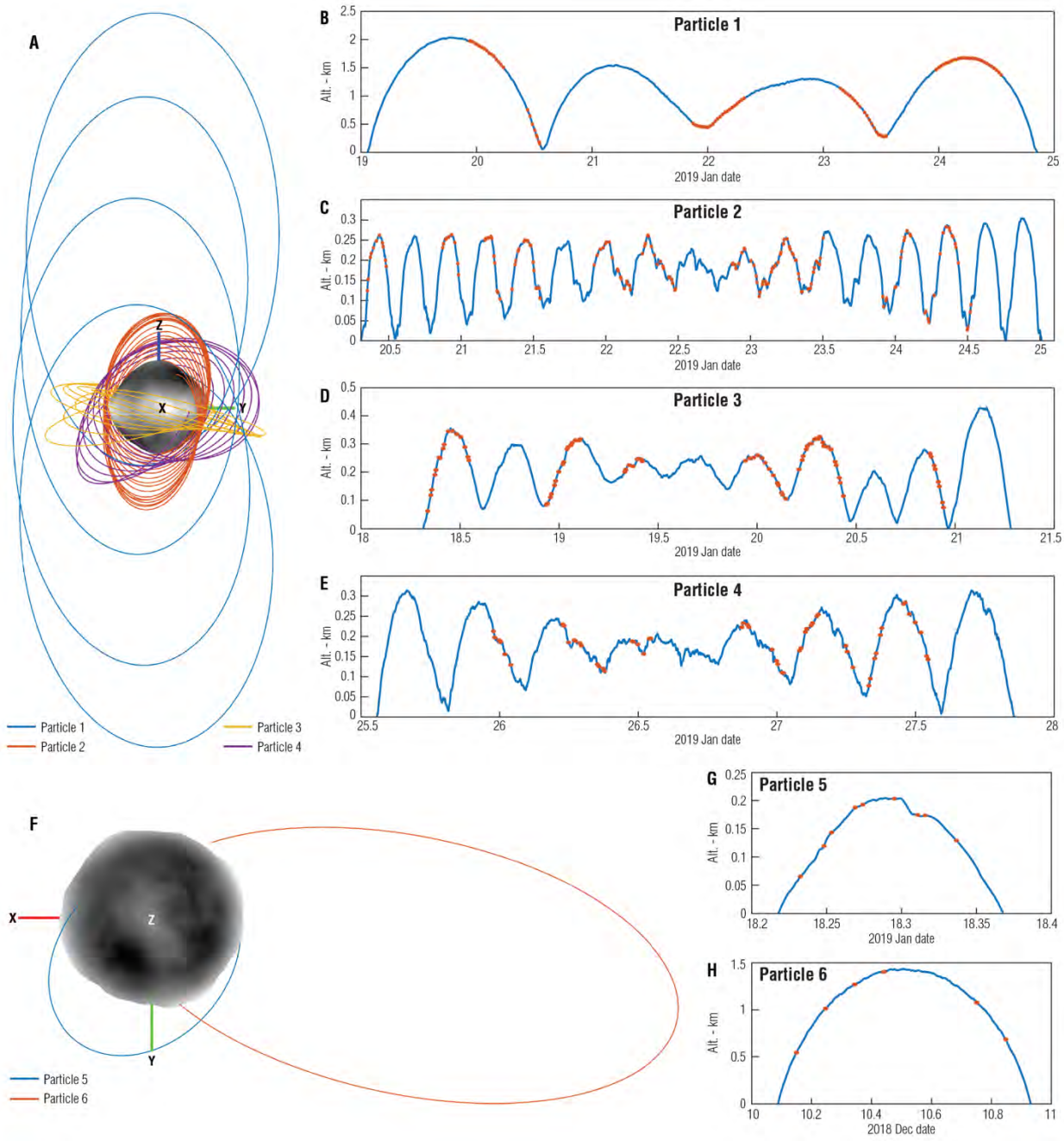

Fig. 4. Gravitationally bound particle altitudes and trajectories. (**A**) Trajectories and (**B** to **E**) altitude above Bennu's surface over time for four orbiting particles (particles 1 to 4; fig. S7 and tables S4 and S5). On the altitude plots, red circles mark the times of observations used in the trajectory estimate. Axis scales of the altitude plots differ. For particles 2 and 3, it is not clear whether the last revolution depicted occurred or whether the particle impacted at the previous

periapsis passage. The ragged appearance of the curves is a result of the rough topography of the surface of Bennu. (**F**) Trajectories and (**G** and **H**) altitude above Bennu's surface over time, as in (A) to (E) but for two suborbital particles (particles 5 and 6; fig. S7 and tables S4 and S5). The trajectories are seen from above Bennu's north pole [*x* axis toward the Sun, *z* axis close to Bennu's north (positive) pole, *y* axis roughly in the direction of Bennu's heliocentric velocity]. Particle 6 is the earliest evidence of a particle in imaging data (10 December).

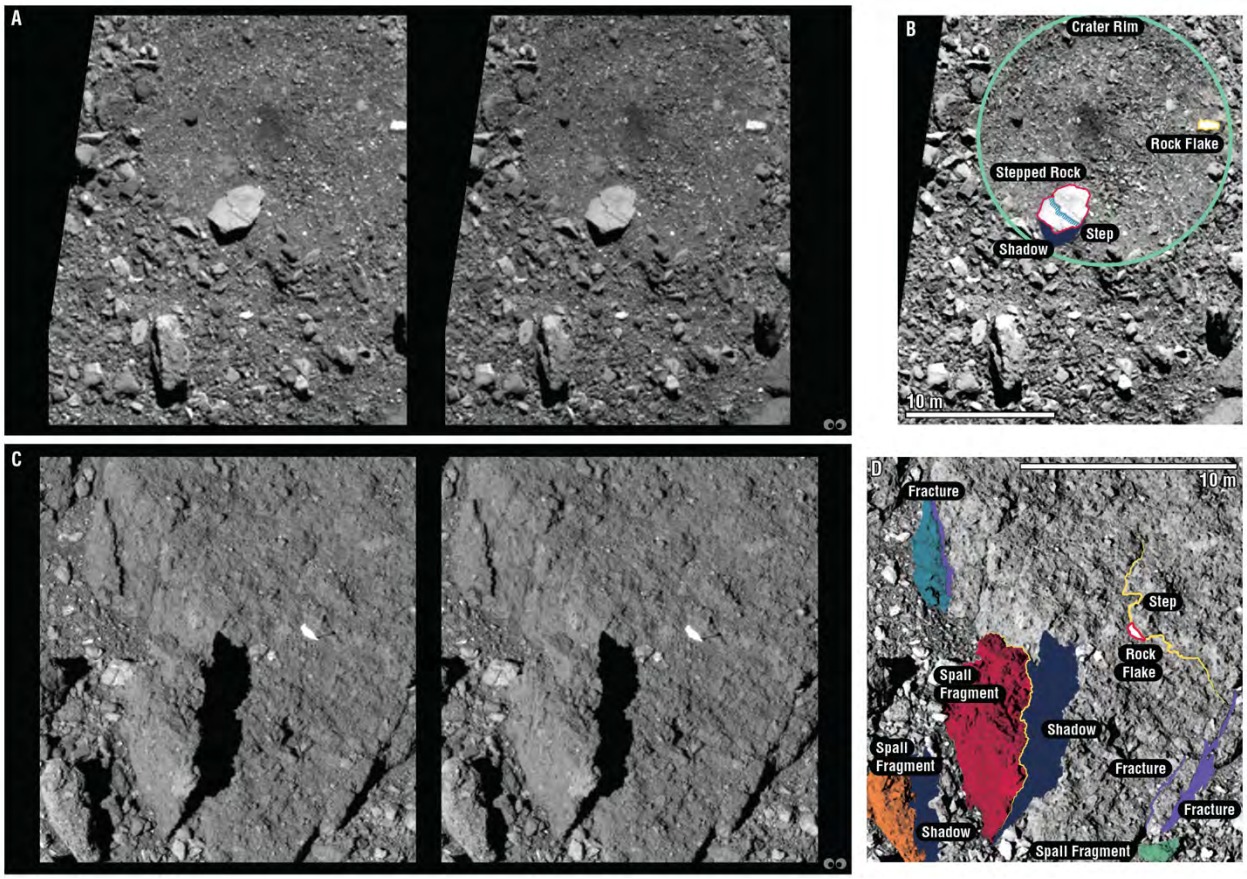

Fig. 5. Two distinct types of exfoliation textures on Bennu. North on Bennu is down. The PolyCam telescopic imager (*12*) acquired the four frames in (A) and (C) while the spacecraft moved with respect to the surface at a speed of 9 cm s^{-1} with exposures of 1/300 of a second (A) and 1/200 of a second (C). These side-by-side stereo images are presented in the stereo "cross-eyed" configuration. A stereoscope-viewing version is available in fig. S10. Each pair of images has been adjusted to match their brightness, contrast, and shadow positions. (**A**) The parallax angle between these two images is 12˚. Phase angle, 44°; pixel scale, 6.6 cm per pixel; (lon, lat), (90°, 11°). (**B**) Annotated version of the image on the right in (A). The large, 5-m white rock on the crater rim displays a flat face, with a well-defined step crossing its center. A white "flake" is present in the upper right. (**C**) The parallax angle between these two images is 8˚. Phase angle, 30°; pixel scale, 4.7 cm per pixel; (lon, lat), (44°, –30°). (**D**) Annotated version of the image on

the right in (C). The large black boulder displays exfoliation textures along both the east and west faces, with fractures running parallel to the texture in the rock. The large rock column in the lower left has a profile that matches that of the step in the boulder, suggesting that this fragment may have been uplifted in an energetic exfoliation event. Even though the rock slab measures 5 by 5 by 1 m, it would only require ~5 J of energy to lift it, assuming a density of 2 g/cm^3. Other spalled fragments are present around the base of the large boulder.

Table 1. Characteristics of the three largest observed particle ejection events. The more extensive imaging datasets acquired for the 19 January and 11 February 2019 events, relative to that for the 6 January 2019 event, allowed higher-fidelity orbit determination (OD) determination of the event locations and times. More detail is given in the methods (*12*) and tables S2 and S3.

	6 January		**19 January**	**11 February**
Number of characterized particles	124 (of 200 total observed)		93 (of 93 total observed)	60 (of 72 total observed)
Velocity range (m s^{-1})	0.07 to 3.3		0.06 to 1.3	0.07 to 0.21
Particle diameter range (cm, ±1σ)	<1 to 8±3		<1 to 7±3	<1 to 7±3
Minimum event energy (mJ, ±1σ)	270 (+150/–225)		100 (+50/–85)	8 (+4/–7)
Event location	Near radiant	Far radiant	OD radiant	OD radiant
Latitude (degrees, ±3σ)	–74.95 (+12.65/–2.79)	–57.30 (+1.49/–17.49)	20.63 ± 0.30	20.68 ± 0.37
Longitude (degrees, ±3σ)	325.32 (+18.91/–10.28)	343.67 (+3.80/–14.73)	335.40 ± 0.09	60.17 ± 0.08
Local solar time (±3σ)	15:22 (+01:06, –00:36)	16:35 (+00:06, –01:05)	16:38:01 ± 00:00:23	18:05:31 ± 00:00:22
UTC time (±3σ)	20:58:28 ± 00:00:47	20:58:28 ± 00:00:47	00:53:41 ± 00:00:04	23:27:28 ± 00:00:06

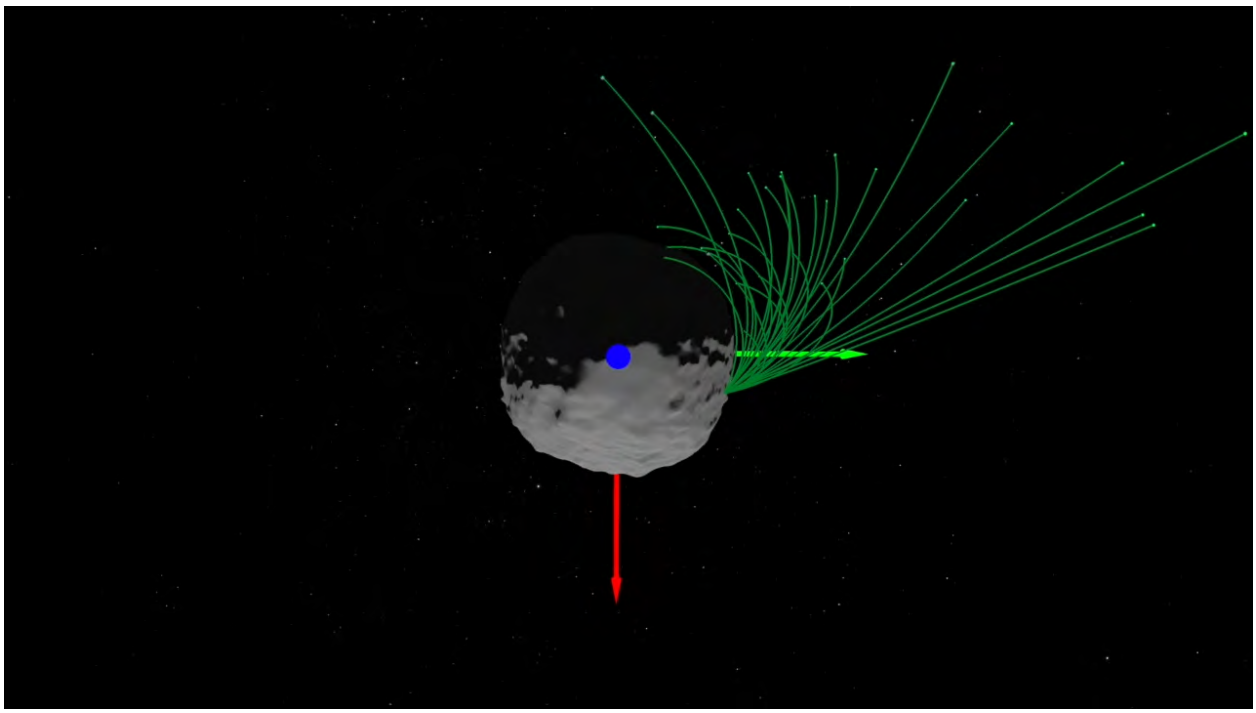

Movie 1. Animation showing the results of the orbit analysis for a subset of the particles ejected from Bennu on 19 January. The highest-velocity particles are on escape trajectories and leave the Bennu environment. Most of the particles are on suborbital trajectories and re-impact the surface, primarily on the night side of the asteroid.

Science
AAAS

Supplementary Materials for

Episodes of particle ejection from the surface of the active asteroid (101955) Bennu

D. S. Lauretta*†, C. W. Hergenrother*†, S. R. Chesley, J. M. Leonard, J. Y. Pelgrift, C. D. Adam, M. Al Asad, P. G. Antreasian, R.-L. Ballouz, K. J. Becker, C. A. Bennett, B. J. Bos, W. F. Bottke, M. Brozović, H. Campins, H. C. Connolly Jr., M. G. Daly, A. B. Davis, J. de León, D. N. DellaGiustina, C. Y. Drouet d'Aubigny, J. P. Dworkin, J. P. Emery, D. Farnocchia, D. P. Glavin, D. R. Golish, C. M. Hartzell, R. A. Jacobson, E. R. Jawin, P. Jenniskens, J. N. Kidd Jr., E. J. Lessac-Chenen, J.-Y. Li, G. Libourel, J. Licandro, A. J. Liounis, C. K. Maleszewski, C. Manzoni, B. May, L. K. McCarthy, J. W. McMahon, P. Michel, J. L. Molaro, M. C. Moreau, D. S. Nelson, W. M. Owen Jr., B. Rizk, H. L. Roper, B. Rozitis, E. M. Sahr, D. J. Scheeres, J. A. Seabrook, S. H. Selznick, Y. Takahashi, F. Thuillet, P. Tricarico, D. Vokrouhlický, C. W. V. Wolner

*Corresponding author. Email: lauretta@orex.lpl.arizona.edu (D.S.L.); chergen@lpl.arizona.edu (C.W.H.)

†These authors contributed equally to this work.

This PDF file includes:

Other Supplementary Materials for this manuscript include the following:

Materials and Methods

OLA off-body detections

The OSIRIS-REx Laser Altimeter (OLA) (*11*) instrument was active on 4 days during the Preliminary Survey phase in December 2018. Each day of observations was broken into two passes of approximately 80 minutes each at a range to Bennu of ~7.5 km and velocities relative to Bennu of 0.2 m s^{-1}. OLA scanned perpendicular to the spacecraft velocity vector with a scan width of ~200 mrad at a rate of ~20 mrad s^{-1}. At the 7.5-km range, these parameters translate into OLA interrogating an area of space of 1.5 km across-track by 1 km along-track. In Bennu-centric coordinates, these linear passes appear as curves and are shown in fig. S1, A to C.

A strict range histogram (not compensating for volume) is expected to be flat, as the probability of a false detection is expected to be equal in range (time) out to a distance of 11.7 km from OLA. The histogram (fig. S1D) shows a peaking of returns given by the two bins between 7 and 8 km where these four detections reside. These calculations do not account for geometric considerations in the plane perpendicular to the nominal OLA pointing direction.

To account for the observational geometry, we calculate the volume of space sampled by OLA. For each half pass and in Bennu-centric coordinates, this volume approximates a triangular prism of length given by the product of the relative velocity with respect to Bennu and the time of observation (~1 km). The width is controlled by the OLA scan angle (~1.5 km). This geometry, along with the assumption of a false detection probability that is uniform in time, allowed the calculation of a relative volumetric probability of observing a false detection as a function of range. This volumetric probability was assigned to each of the 21 off-body returns.

A histogram of the volumetric probability for each off-body return as a function of range from the center of Bennu is used to calculate a relative confidence in the off-body returns representing real objects (fig. S2). Each bin of the histogram represents a spherical shell of a volume that scales by the square of the range. At larger ranges, the overlap between the volume of space sampled by OLA and the spherical shell is not complete. The volume used for each bin in fig. S2 is that of the overlap between these two volumes. Using these volumes and the volumetric probability calculated for each return, the histogram was scaled by the inverse of the calculated probability of detection and normalized to the largest bin. This results in the histogram of fig. S2, where the four returns are represented by the two highest-confidence bars. This result supports the conclusion that the four detections in question are, with high probability, returns from off-body objects. Further evidence is provided by a conic trajectory model fitted to the third and fourth points, which results in an orbit similar to those of the subsequently discovered orbiting particles.

NavCam 1 optical navigation instrument specifications

The NavCam 1 camera is part of the OSIRIS-REx Touch And Go Camera System (TAGCAMS) (*13*). It uses a seven-element all-refractive lens with a nominal focal length of 7.6 mm. The camera contains the ON Semiconductor (formerly Aptina) MT9P031 5-megapixel image sensor with 2592 × 1944, 2.2-micron pixels and on-chip 12-bit digitization. The detector and optics produce a field of view of about 44° × 32° and an on-axis pixel scale of 0.28 mrad per pixel or 58 arc seconds per pixel. The majority of NavCam 1 particle images were taken with an

exposure time of 5 s, producing a point source limiting magnitude of $V \sim 7$. The cadence of NavCam 1 imaging is given in table S1.

NavCam 1 image analysis

Production of NavCam 1 ejection event images

We produced the asteroid particle event visualizations shown in Fig. 1 by combining multiple sub-frames from a single long-exposure (5.0 s) image of Bennu with a short-exposure (0.001376 s) image of the same (fig. S3). The short-exposure image that we select is the one with identical spacecraft pointing and is closest in time to the long-exposure image in which particle ejections are detected. The time between the two exposures is 9.9 s for 6 January and 9.4 s for 19 January.

We first create a median-filtered version of the long-exposure image by applying a square median filter, 13 pixels wide, to the long-exposure image. Then we subtract the resulting median-valued, long-exposure image from the original long-exposure image to create a median-filtered image. This process removes the image digital number (DN) offset, the dark current, and the median stray light in a 13-pixel-wide sub-window. Next, we sort through the median-filtered image to extract sub-frames centered on pixel coordinates identified by the Goddard Image Analysis and Navigation Tool (GIANT) software (*57*) as the positions of unknown and uncatalogued sky objects in the original long-exposure image. At each object's location, we extract an 11 × 11 pixel sub-frame from the median filtered image and assign at the same pixel coordinates the DN values to a null array the same size (2752 × 2004) as the short-exposure image. This creates an array of mostly zeros with 11 × 11 sub-frames scattered throughout that record the median-filtered DN values from objects judged to be uncatalogued by GIANT. We use an 11 × 11 pixel sub-frame size based on the in-flight measurements of the NavCam 1 point spread function.

After we finish populating the null array with sub-frames containing the DN values from the uncatalogued objects identified by GIANT, we replace each pixel value in the array with the square root of its original value. This type of non-linear, DN-histogram stretch exaggerates the DN values of the dimmer objects to make them more visible. To bring out the dimmest objects even more, we threshold the square-root image at 20 DN (for a 12-bit image) above the median background, which forces the brightest objects to have identical peak DN values. This thresholded, square-root image's histogram is then linearly stretched so that the maximum DN value in the image matches the maximum DN value in the processed long-exposure image. This process produces non-linear radiometry within and across the object sub-frames but maintains the correct qualitative intensity relationship between objects (except for the brightest pixels with threshold DN values that are identical).

The short-exposure image processing involves only a few steps. First, we remove the DN offset and mean dark current from the image and threshold the resulting array on the low end of the DN histogram such that the remaining minimum DN value equals zero. Next, we threshold the high end of the DN histogram at one-quarter of the peak DN value to bring out the darker regions of the Bennu image. The actual DN value depends on the short-exposure Bennu observing conditions, but we use the maximum value that is selected to threshold the high end of the sub-frame array's DN histogram.

After processing the long-exposure image and creating the sub-frame array, we combine the two via summation. This produces a composite image with DN values at most pixel locations identical to those of the processed long-exposure image except for those positions where GIANT finds unknown objects. Even though the unknown object signals are about 3000 times dimmer than Bennu's surface, the independent image stretches and approximate histogram matching allow both types of features to be visible in a single image frame.

Stray light reduction

All NavCam 1 particle images include all or a part of the spacecraft-facing hemisphere of Bennu. With exposure times of 5 s, the sunlit portion of Bennu is saturated. The brightness of Bennu also affects the rest of the NavCam 1 field of view with varying levels of stray light. A variant of the classical unsharp masking was used to remove the stray light to increase the contrast between faint particles and the image background using the IRAF (Image Reduction and Analysis Facility) CCDRED package (*58*). In this process, a copy of the image is convolved with a Gaussian kernel of 3 pixels. The original image is then divided by the convolved image. This technique is commonly used in planetary astronomy to enhance the visibility of fine features within the coma of bright comets (*59*). This technique is efficient at removing diffuse features, as would be expected for clouds or plumes of unresolved dust. We used this technique to create fig. S4.

Differencing of images

OpNav analysis of NavCam 1 images for particles involves the differencing of two images closely spaced in time. Differencing is accomplished by subtracting the first image in the sequence by the later image. The differencing technique removes all sources that are not moving relative to each other. Before image subtraction, it may be necessary to register the images on the stellar background so that the stellar sources are located at the same *xy* pixel coordinates. Objects moving relative to the stellar background, such as particles, produce positive-negative pairs in the resulting differenced image. This is another technique that has been used to enhance near-nucleus comet features and the detection of moving asteroids (*59*).

Particle detection

The identification of particles in NavCam 1 images was accomplished using a combination of methods. The GIANT software identified point sources in each image that did not correspond to background stars. Visual inspection of these unidentified point sources was independently conducted in KXIMP (KinetX Image Processing) (*60*, *61*) and the ds9 FITS (Flexible Image Transport System) image viewer (*62*) to verify whether they were Bennu-related particles, high-energy particle artifacts, or hot pixels on the detector. NavCam 1 images were further inspected in ds9 and KXIMP to identify particles not flagged by GIANT. KXIMP and ds9 were also used to identify and characterize particle streaks, which GIANT does not nominally identify.

Ejection event orbit determination

Images that contained ejected particles were analyzed using OpNav techniques to determine the particle size and states, as well as time and location of surface ejection. The first two images taken by NavCam 1 following a given event were corrected for distortion and registered on the center of Bennu; they were then differenced so that particle motion with respect to Bennu would be perceptible upon blinking pairs of images in ds9. Stars all have the same apparent motion,

making them readily distinguishable from particles. A particle distribution pattern near the limb of Bennu in the first image is apparent farther from the limb and dispersed in the second image. We associated pairs of detections (tracks) from this pattern. Fast-moving particles cross multiple pixels in a single exposure and occur as trails or streaks in images, providing position and velocity information within each such image (fig. S5). It is apparent from this initial association of tracks in the image plane that the particles originate from a single, discrete radiant location on the asteroid surface (Fig. 1, B and D).

The radiant locations and epochs (times of ejection) were determined by making measurements in the image plane. We first estimated the common radiant point of each event by performing a least squares estimation of the intersection point of all the lines connecting the two sets of observations in the image plane. We used the root-mean-square distance from each line to the estimated radiant point to obtain the 1σ uncertainty.

The time each object left the radiant point was estimated by comparing the angular displacements of the object from the radiant at each detection time. In cases with only two image detections, the radiant epoch for the event is degenerate, and it is coupled with ambiguity in the orientation of the ejecta cone. However, for three- or four-detection tracks, or where there are streaked objects captured in one or both of the images, we use a more robust method to determine the time that each object left the radiant point. A three-detection track allows for a deterministic solution of the epoch that removes the 3D track orientation ambiguity. For four-detection tracks, we obtain multiple radiant epoch estimates using different combinations of three detections each for the track. We constrain the time of each event using the median of the times estimated from each individual object, and we use the standard deviation of the times for the 1σ uncertainty.

With the epoch thus constrained, we use the ray-tracing routines in the NAIF (Navigation and Ancillary Information Facility) SPICE (spacecraft, planet, instrument, constants, and events) toolkit (*63*) to determine the 3D surface location of the ejection event. This yields two solutions for the origin point on the surface of Bennu along the spacecraft-to-radiant vector: an origin on the near side of Bennu (closer to the spacecraft) and an origin on the far side of Bennu (out of the camera's view). To obtain the near-point solution, we trace rays from the spacecraft's location at the time when the first image was obtained back toward the estimated radiant point until they intersect with the Bennu shape model [described in (*64*), wherein the coordinate system is also given], using the rotation state of the asteroid at the event epoch. For the far-point solution, we place the vertex along the spacecraft-to-radiant vector, but on the opposite side of the asteroid, and trace the ray back toward the spacecraft. To determine the uncertainty in the location of the estimated origin points on Bennu's surface, we sample the pixel-space radiant point uncertainty and the event time uncertainty at their 1-, 2-, and 3σ values, then repeat the ray-tracing. We validate this approach by using the Mersenne Twister Monte Carlo (*65*) function in MatLab to sample the simple Gaussian distribution of the event times and pixel-space radiant point (described above) and input these into the NAIF toolkit to independently calculate the 1-, 2-, and 3σ contours. The results of these analyses provide initial constraints on the location and time of the particle ejection events (Figure 3, Table 1, and table S2).

For our initial assessment, we infer initial 3D object states by assuming that there were no accelerations acting on the particles and that every object left the radiant point instantaneously. We inferred that objects appearing faster than expected were closer to the camera, and those appearing slower than expected were farther away. We combined this information with the two possible locations of the radiant point on the surface of Bennu to determine the 3D position of each object. We then calculate the corresponding velocities using the position of each object at the two image times.

We expand on the initial assessment by performing a more rigorous analysis of particle trajectories using orbit determination (OD) techniques implemented in MIRAGE (Multiple Interferometric Ranging and GPS Ensemble) (*66*, *67*), now called MONTE (Mission Analysis, Operations, and Navigation Toolkit Environment) (*68*). For the 6 January dataset, the event radiant is at a high southern latitude, and its orientation relative to the spacecraft makes estimating the true latitude difficult. Our ability to fully estimate the particle trajectory and origin location is limited by the lack of more than two detections for the particles and the geometry of the event as seen from the spacecraft; the OpNav solution is the best available.

In the better-observed cases of the 19 January and 11 February events, this additional analysis allows us to uniquely identify the near or far radiant as the source location of the ejection events. This process starts by performing an initial OD for each observed particle using a traditional "angles-only" technique (*69*). In this technique, image data are converted from pixel-line coordinates to right ascension and declination from the spacecraft in the inertial reference frame. This frame defines a unit vector from the spacecraft to each observed particle. When only two observations are available for a single particle, there are four observations (two sets of right ascension and declination) and six unknowns necessary to estimate the full state of the particle's trajectory (three components each of position and velocity); this produces an indeterminate system. However, when at least three particles are detected in two sets of images each, the system is well constrained by 12 observations with 12 unknowns (the three components of velocity for each particle and the three components of radiant position common to all the particles). Under these circumstances, it is possible to estimate the location of the ejecta radiant with conic trajectories. We assume that the particles followed a conic orbit that was not influenced by any force except point-mass gravity. We also make the assumption that each radiant is on Bennu's surface, allowing us to use the shape model to constrain the ejection location. Any greater number of particles or observations allows for an overdetermined system to be solved multiple times, providing an assessment of the intrinsic spread in radiant location and epoch.

We did not include solar radiation pressure (SRP), thermal emission from Bennu, or gas-drag forces in these OD solutions. Because the arc length is short for each particle, we determined that the potential error introduced did not substantively affect the reconstruction of the trajectories over the several hours of the observations. As discussed below, these additional small forces become non-negligible when modeling longer-duration, gravitationally bound particle trajectories that persist for days.

Particles on short-lived orbits

Recognizing and analyzing particle trajectories requires linking individual detections to form datasets associated with a given object. Methods to resolve this problem exist for the relatively simple dynamics of asteroids [e.g., (*70*, *71*)], but can be more complex when the dynamics are not smooth or additional forces contribute to the trajectory, as apply in the case of particles ejected from Bennu.

The smallest unit of data for orbital fits is the track, which includes at minimum two right ascension–declination positions, making it possible to infer the plane-of-sky position and velocity. Additional detections can sometimes be associated to form a track of more than two detections, and multiple tracks can be gathered to form a longer arc of observation. Linkage efforts have taken place either in orbital elements space or on the spacecraft plane of sky. In the former case, where a single track provides enough information to derive a preliminary two-body (conic section) orbit, multiple tracks can be connected by virtue of obvious similarity among the orbital elements. This is particularly effective when each track includes enough data (about four to six detections over 1 to 2 hours) to infer reliable orbital elements and when the various tracks are close enough in time that the evolving orbital elements (table S4 and fig. S7) have not changed so much as to obscure the association. Alternatively, orbits from individual tracks, either from conic sections or fitting with the full dynamical model, can be projected onto the spacecraft plane of sky. In that frame, linkages can be inferred by the similarity of position and velocity among unlinked detections and the orbital predictions. This approach re-fits an orbit with a full dynamical model after adding in newly linked detections, which allows predictions to be more robust so that linkages more distant in time become possible. The result is a series of tracks that can be fitted to a short-lived orbit.

The known forces affecting the trajectories of particles in Bennu's environment are gravity and radiation pressure. In the presence of only gravitational forces, particles ejected with less than the escape velocity, which ranges between 10 and 23 cm s^{-1} across the surface (*16*), will tend to return to the surface because the periapsis is below the surface at ejection. Radiation pressure effects acting after ejection can subsequently alter the orbit so that the particle clears the surface after the first revolution. In the simplest case, this occurs when the orbit is oriented so that when the particle is at apoapsis, SRP is increasing the orbital velocity. This increasing velocity will raise the periapsis distance, and in some cases the particle will pass above the surface at the first periapsis. This process continues until the orbit is near-circular, at which point the process typically reverses when the periapsis flips to the other side of the asteroid and SRP begins to reduce velocity at apoapsis, thus lowering periapsis distance until it falls below the surface and the particle re-impacts.

Particle trajectory estimation is based on a series of RA-DEC angular measurements from the OSIRIS-REx spacecraft. Our trajectory estimation relies on classical orbit determination algorithms as previously implemented in (*72*). We also made use of the SPICE software suite using kernels publicly available on the NAIF website (*73*). The reduction and processing of angular position measurements is covered by (*74*), the propagation of trajectories and treatment of time is described by, among others (*67*), and the estimation approach that we use is that of (*75*).

We observe particles spending extended periods on low-altitude orbits within 300 m of the surface, and in this regime, the trajectories are strongly influenced by the mass distribution within Bennu (Fig. 4). A variety of models exist for describing and estimating the gravitational forces acting on a particle. The most frequently used tool for gravity science is the spherical harmonic expansion, which is poorly suited to our problem given that the particles spend considerable time well within the circumscribing sphere of Bennu, where the spherical harmonic expansion is not guaranteed to converge and thus is a poor model for the gravitational acceleration (*76*, *77*). An alternative is the polyhedral gravity field, which provides the exact gravitational acceleration for a given polyhedral shape model (*78*). However, the standard polyhedral model assumes a uniform material density within the body, which is not the case for Bennu (*16*). Our models rely on these two approaches. In addition to Bennu's gravity, we include the gravitational (tidal) perturbation from the Sun.

Radiation pressure acting on the particles arises from a number of sources, with the predominant source being direct solar radiation, so we must consider the timing of entry and exit from Bennu's shadow. We based this on the mission-derived shape model (*64*). Other radiation sources include thermal radiation and reflected sunlight from the surface of Bennu, for which we perform a facet-by-facet sum of the force, again using the mission-derived shape model. The Bennu temperatures used to compute the thermal radiation pressure are based on thermal measurements taken during the approach to the asteroid (*17*). Our approach to modeling radiation pressure is to estimate the area-to-mass ratio of the particle, which constrains the mean cross-sectional area of the (presumably tumbling) particle that is exposed to radiation.

Each of these three input radiation sources (solar, thermal, and reflected sunlight from Bennu) leads to combined radiation pressure effects due to photons reflected from the particle, which can be more difficult to model given the unknown physical properties of the particle. In the absence of detailed information on the optical properties of the particles, we assume that particles are Lambertian scattering spheres, which implies that the ratio of reflected to direct radiation pressure is $(4/9)p_V$, where p_V is albedo in the V band. Taking the additional assumption of 10% albedo implies that the reflected radiation pressure is 4.4% of the direct radiation pressure, which informs our area-to-mass ratio values tabulated in table S5. We neglect thermal emissions from the particle under the assumption that it is isothermal by virtue of rapid rotation and small size. With these assumptions, we can estimate the area-to-mass ratio when modeling the radiation pressure in the presence of a well-characterized radiation source.

Particle trajectory model fits indicate a small effect of additional forces not accounted for in the model. These small forces arise from three potential sources: non-spherical effects, mass loss from the particles, and gas drag. Reflected SRP depends on the unknown albedo of the particle; non-spherical effects can deflect the net reflected pressure off the Sun line, leading to a component of acceleration orthogonal to the Sun direction. Radiation pressure from Bennu is only ~10% of that from SRP, so reflected solar radiation dominates the reflected radiation modeling problem. Another possible source that cannot be ruled out is acceleration due to mass loss from the particles caused by particle outgassing or fission. These two forces have different signatures and may be separable; a combination of both could be at play. Force modeling ambiguities affect the uncertainties on other estimated parameters (e.g., gravity and area-to-mass

ratio). Thus, although we provide uncertainties on some estimated parameters, these are intended as an indication of a scale rather than a rigorous assessment of uncertainties.

We considered drag from gas emitted by Bennu as a possible source of particle acceleration. The additional forces noted above appear to be acting at all distances, from near surface to more than 1 km from Bennu, which is inconsistent with the radial dependence of gas drag. Furthermore, modeling of the OSIRIS-REx spacecraft trajectory, which orbited at a radial distance similar to that of particle 1 (Fig. 4), shows that SRP is at least a factor of 50 greater than all other small forces (*79*). Thus, any gas drag effect would be negligible.

OCAMS image analysis

Production of OCAMS images

Fig. 3 shows polygons of the ejection sites overlaid on a mosaic of images acquired by the PolyCam imager of the OSIRIS-REx Camera Suite (OCAMS) (*80*). To create the mosaics, we used radiometrically calibrated PolyCam images acquired at low emission angles (<20°) during Flyby 3 (21 March 2019) and Flyby 4 (28 and 29 March 2019) of the OSIRIS-REx Detailed Survey Baseball Diamond imaging campaign, with an approximate median pixel scale of 5.25 cm per pixel (*81*). Images were projected to a tessellated 3D shape model (v20) of Bennu (*64*) and mosaicked using an equirectangular map projection with the Integrated Software for Imagers and Spectrometers version 3 (ISIS3) (*82*); the mosaicking techniques and procedures used to create the final product are described in (*81*). The phase angle is ~40° for panel A and ~30° for panels B and C.

Fig. 5A consists of PolyCam images 20190404T185209S216_pol and 20190404T190045S849_pol acquired on 4 April 2019. Fig. 5C consists of PolyCam images 20190321T202442S482_pol and 20190321T203026S529_pol acquired on 21 March 2019. OCAMS PolyCam images are calibrated into units of reflectance (*I/F*) (*17*).

Normal albedo of source regions

We calculate the albedo of the event source regions using a normal reflectance map of Bennu's surface, created using data taken during Flyby 1 (7 March 2019). Flyby 1 data were taken with very short exposure times to avoid saturation, which produce icicle-shaped artifacts in the images. Those artifacts limit the efficacy of the charge smear correction and result in >10% radiometric variation from image to image. We correct this variation by radiometrically and photometrically controlling the Flyby 1 mosaic to a lower-resolution, panchromatic, normal reflectance map created using MapCam data from the Equatorial Stations imaging campaign (9 May 2019). This correction reduces albedo uncertainty to less than 5%. We calculate the histogram over the pixels contained within the geographic footprints of the source regions. The footprints, specified in latitude and longitude coordinates, are defined by the radiant location (Fig. 3) and associated 3σ uncertainties (covering about 500 projected pixels for each source region).

Production of stereo images

For stereo image processing (Fig. 5 and fig. S10), pairs of Bennu surface pictures are selected from the highest-available-resolution images, based on suitable stereoscopic parallax and

avoiding shadow discrepancies as much as possible. The original images are rotated and cropped to show the same portion of interest of Bennu's surface. The images are then combined into a stereo view, bringing the images to a common scale, aligning them and cropping a preliminary stereo window. The brightness, contrast, and color are adjusted to match the histograms between the two images. Optimizing the image pair involves adjustments to the rotation of each image to finetune the parallax to be horizontal, needed for optimum stereo viewing. In some cases, a global correction for distortion is applied to correct for different angles of view in the component images. In most cases, we correct for the differences in shadows that result from the phase angle of the Sun having changed between exposures. Because the exposures are chosen from a single pass, in the time taken for the camera to move sufficiently to produce a workable baseline, the asteroid had rotated enough to produce shadow problems in the stereo pair. Correction for these discrepancies has to be done shadow by shadow. Shadow information from one component image is copied to the other, but modified according to the different parallax involved and the terrain upon which the shadow falls. After these adjustments, the images are cropped again because the fine adjustments to relative orientation produce losses at the edges.

Photometric analysis

Photometry was conducted using two separate tools utilizing two different photometric techniques. Aperture photometry of the 6 January, 19 January, and 11 February particle ejection events was conducted using the DIGIPHOT tool within the IRAF suite (*58*). Photometry was conducted on the original NavCam 1 images prior to stray light subtraction and image differencing.

Three different combinations of photometric apertures and sky background annuli were used depending on the apparent velocity of the particles (i.e., the amount of trailing across pixels). For particles that appeared as point sources, a photometric aperture with radius 5 pixels (~5′) and sky background with inner radius 5 pixels (~5′) and outer radius 10 pixels (~10′) was used. Most trailed objects were measured with a photometric aperture of radius 10 pixels (~10′) and sky background with inner radius of 10 pixels (~10′) and outer radius 15 pixels (~15′). The particles with the fastest apparent velocities were measured with a photometric aperture of radius 30 pixels (~30′) and sky background with inner radius of 30 pixels (~30′) and outer radius 35 pixels (~35′). Total DN counts measured within the photometric aperture were converted to V-band apparent magnitude m_V via

$$m_V = \left(\frac{1}{a}\right) * log10(DN/t * 1.25/(g * c)) \qquad \text{eq. S1}$$

where, for NavCam 1, a = –0.40362, c = 31564.2, g = is the commanded gain (1.25), DN is the total DN measured in the photometric aperture, t is exposure time in seconds (5 seconds), and log10 stands for the base 10 logarithm.

Particles within ~30 pixels of the saturated limb of Bennu were not measured due to the noise produced by stray light. A photometric correction was applied to saturated particles to compensate for the DN lost due to saturation. A study of bright stars in the NavCam 1 fields found that saturation started producing a loss in measured brightness above a V-band apparent magnitude of ~2.4. The brightest measured particle produced a “saturated” apparent brightness

of magnitude 1.84. A correction of 0.53 mag was applied to produce a true apparent magnitude of 1.31.

The linear phase function is determined by normalizing the apparent magnitude for each photometric measurement to particle-Sun and particle-spacecraft distances of 1 au. A linear regression is determined for the phase angle and normalized apparent magnitude dataset. Unique linear phase functions were determined for particles 1 to 3. Phase function solutions for particles 4 to 6 were ambiguous due to limited phase angle coverage and low signal-to-noise photometry. The photometry of particles 1 to 3 were conducted at phase angles between 73° and 110° and resulted in a mean linear phase function of 0.018 ± 0.005 mag per degree of phase angle. The particle phase functions were considerably shallower than the mean disk-integrated phase function of Bennu (*10*) and asteroid phase functions (H-G, H-G12, H-G1-G2) (*83*) fitted to the particle photometry.

Absolute magnitudes and uncertainties are listed in table S5. The 1σ uncertainties are on the order of ±0.4 mag for particles 1 to 3 and ±0.8 mag for particles 4 to 6. The error analysis included the uncertainty in the individual linear phase function solutions, as well as non-linearity in the extrapolation to 0° phase angle such as an opposition effect. A range of 1.6 mag (±0.8 mag, 1σ) corresponds to a difference of ~4.4 in projected area or a factor of ~2 in diameter. While the properties of the particle phase functions are unknown for phase angles <73°, the uncertainties are consistent with all objects being sub-centimeter to centimeter-scale particles. The upper limit of observed particle diameters (particle 6 and largest particle from the January 6 event) is 8 ± 3 (1σ) cm for an albedo range of 0.033 to 0.15, the normal albedo range observed on the surface of Bennu.

The mean linear phase function is used for all other particles, including those in the ejection events (due to a lack of sufficient observations to determine phase functions for each particle). Extrapolation of the phase function to a phase angle of 0° produces the absolute magnitude (brightness of an object at 0° phase angle and 1 au from the Sun and observer) (table S5). Absolute magnitude can be converted into the diameter of an assumed sphere using (*84*)

$$D = \frac{1.329 \times 10^8}{\sqrt{p_V}} 10^{-0.2 H_V} \qquad \text{eq. S2}$$

where D is the particle diameter (in centimeters), p_V is geometric albedo, and H_V is absolute magnitude in the V band. Sizes are then converted to the volume of a sphere and mass assuming a density of 2 g cm^{-3}. The kinetic energy equation is used to calculate the kinetic energy of each particle from the measured velocity and mass. The sums of the individual particle masses, volumes, and kinetic energies produce the total masses, volumes, and kinetic energies of each large event (table S3). Values are shown for four different albedos: 0.033 (representing the darkest material seen on the surface of Bennu), 0.044 (global mean average), 0.07, and 0.15 (representing the brightest material) (*19*, *17*). We use the global mean average albedo to determine the minimum event energy (Table 1 and table S2), and the range of albedos to determine the 1σ uncertainties.

Only a subset of the observed particles has trajectory information. For those particles with photometry but no trajectories, the mean velocities, ranges, and phase angles determined for each individual event were used.

Roche lobe computation

The computation of the rotational Roche lobe, a description of the detailed surface slope structure, and the average radius of Bennu as a function of latitude are described in (*16*).

Ejection event contribution to Yarkovsky effect and rotational acceleration

To compute the possible contribution of particle ejection to the Yarkovsky effect, we compute a simple analysis; for the rate of change of the Bennu spin rate, two different approaches are taken, one qualitative and the other a more quantitate averaging approach based on the shape model of the asteroid across a range of possible particle ejection speeds. For all approaches, we use the estimated values for the asteroid total mass of 7.329×10^{10} kg, polar moment of inertia equal to 1.964×10^{15} kg m^2, current spin period of 4.296 hours, and spin rate acceleration of 3.63×10^{-6} deg day^{-2} (or 8.487×10^{-18} rad s^{-2}) (*16*, *64*, *10*). For a "canonical" ejected particle, we assume a sphere of diameter 10 cm and density of 2 g cm^{-3}, yielding a mass of about 1 kg. The escape speeds across the surface of Bennu range from 10 to 23 cm s^{-1}, depending on the orientation of the surface and incorporating the rotation of the asteroid (*16*). For an ejection from the volume-averaged radius of Bennu (245 m), neglecting rotation, the escape speed is 20 cm s^{-1}.

For the Yarkovsky computation, given an ejected particle of mass m and speed v, the corresponding change in the asteroid's speed will be $V' = \frac{-m}{M} \times v$, where M is the asteroid's mass. Thus, a particle ejected at 1 m s^{-1} will change the asteroid's speed by ~1×10^{-11} m s^{-1}. Compared to the computed Yarkovsky acceleration, this is equivalent to ejecting one particle every 5 s (in the correct direction), or about 18,000 particles per day.

For the rotational computation, when a particle is ejected from the surface, the entire system of Bennu plus particle will conserve angular momentum. Thus, if the particle returns to Bennu's surface, the spin rate will only be adjusted depending on whether the mass movement associated with the particle has changed the polar momentum of inertia of the system (neglecting complex rotation), which is generally a small effect. However, if the particle escapes directly, then it takes with it the angular momentum it had when initially ejected from the surface. To model this, we assume that the moment of inertia of Bennu plus the particle is $I + mR^2$, where I is the Bennu polar moment of inertia, m is the particle mass, and R is the Bennu radius at which the particle is ejected. The entire system spins at a rate Ω, leading to the total angular momentum $H = (I + mR^2)\Omega$. After ejection, the total system angular momentum is conserved, but Bennu has a new spin rate Ω', and the ejected particle has an angular momentum component relative to the rotating system and along the rotation axis of $m\hat{\boldsymbol{z}} \cdot (\boldsymbol{R} \times \boldsymbol{V})$, where **V** is the surface relative ejection velocity vector and $\hat{\boldsymbol{z}}$ is the rotation pole direction in inertial space. The total angular momentum is then $H = I\Omega' + m\left[R^2\Omega + \hat{\boldsymbol{z}} \cdot (\boldsymbol{R} \times \boldsymbol{V})\right]$, and when balanced with the initial angular momentum we find $I(\Omega' - \Omega) = -m\hat{\boldsymbol{z}} \cdot (\boldsymbol{R} \times \boldsymbol{V})$. Thus, if the particle escapes without further gravitational interactions with Bennu, this represents the net change in rotation rate of the asteroid. If the ejection rate is less than direct escape, and the particle and asteroid exchange

angular momentum, the net change in rotation rate is more complex (*85*). This analysis neglects the effect of ejection angular momentum components perpendicular to the spin axis.

Given this expression, we can compute the effect of ejecting a particle along the equator. If a 10-cm particle is launched tangent to the surface (assuming a radius of 245 m) at a surface relative speed of 1 m s^{-1} (which guarantees direct escape), the change in rotation rate will equal about $\pm 1 \times 10^{-13}$ rad s^{-1}, depending on if the particle is ejected to the west (+) or east (–). We can compare this to the measured rotational acceleration of Bennu and note that an ejection of one such particle every 15,000 seconds (or about six times per day) in the westward direction can account for the measured rotational acceleration. Thus, it is clear that particle ejections can contribute to the asteroid rotational acceleration. However, if ejections are considered to occur randomly across the Bennu surface, we would not expect such a systematic effect. First, these ejections would tend to cancel each other to some extent depending on the ejection direction, and second, due to the rotation of Bennu, we would expect particles ejected to the east to escape at slower speeds, and hence preferentially "drain" angular momentum away from the asteroid and reduce its spin rate. This has been considered (*50*) with regard to the preferential escape of low-speed ejecta from a rotating asteroid. The mechanics of this process are different for particle ejections, however, and must be computed in more detail for the specific shape of Bennu.

To do this, we use the concept of the guaranteed surface escape speed [chapter 10 of (*86*)]. This is the speed that a particle ejected normal to the surface of an asteroid must have to directly depart on a hyperbolic orbit. It is computed accounting for the rotation of the asteroid and for the non–point-mass gravitational potential of the asteroid. A particle launched at or beyond this speed will escape the system; however, a particle launched at a lower speed may still escape, but it would have to undergo repeated interactions with the asteroid over multiple orbits before escape could occur, which would complicate our simple angular momentum budget. Here we assume that particles launched at lower speeds will eventually fall back to the asteroid surface. Then, under the assumption that any region of the asteroid surface might eject a particle, we can compute the net change in spin rate for particles ejected at a given speed normal to the asteroid surface at every point. For very slow ejection speeds, no particles escape, and thus there is no change to the asteroid spin rate. As the ejection speed is increased, only some of the particles will escape—those preferentially ejected towards the east—and thus we expect a decrease in the asteroid spin rate. For a large enough ejection speed, all particles will escape, and the expected net change in spin rate will go to zero again. Figure S11 shows the net change in spin rate per kilogram for particles launched at a given ejection speed uniformly from the entire Bennu surface. Multiplying the resultant number by the particle mass flux in kilograms per second will yield the effective rotational acceleration due to uniform particle ejection. For an ejection speed below the minimum direct escape speed, this shows a zero change in spin rate. As the ejection speed increases, the most likely ejections are towards the east, which gives a net decrease in spin rate. This is maximized at an ejection speed of about 18 cm s^{-1}, controlled by when ejection toward the west becomes possible. Finally, when the ejection speed is greater than the maximum ejection speed, we find a total net zero change again. This is expected as the asteroid is then uniformly radiating particles from its surface. For an optimal ejection speed of 18 cm s^{-1} and an escaping mass flux rate of 2 kg day^{-1}, we find that the maximum net decrease in Bennu spin rate is ~0.25% of the measured rotational acceleration. At this ejection speed, particles will escape from approximately half of the surface. Thus, to change the rotational acceleration by 1% of its

current value per day, Bennu would need to eject material at a flux of approximately 8 kg day^{-1}, which can be done with approximately twenty 10-cm particles.

Surface and subsurface temperature calculations

Temperatures on Bennu are computed using a version of the Advanced Thermophysical Model (ATPM) (*87–89*) customized for the OSIRIS-REx mission (*17*). The model explicitly captures shadowing, self-heating, multiple scattering, and visibility of surface facets as defined by the topography of the shape model. The same effects caused by roughness at spatial scales smaller the shape model resolution and larger than the thermal skin depth (~2 cm) are modeled by spherical section craters. We use the thermal inertia (350 ± 20 J m^{-2} K^{-1} $s^{-1/2}$) and roughness (RMS slope 43 ± 1°) determined from disk-integrated Approach-phase observations (*17*) and assume these quantities are constant across the surface and with depth. The temperatures are sensitive to local topography; incidence angle and shadowing are the primary controls on energy input. We therefore use the highest-available-resolution global shape model, which has a resolution (facet size) of 75 cm and contains ~3 million facets. Temperatures are computed over an entire orbit of Bennu around the Sun to determine the maximum temperature for assessing volatile stability.

Re-impacting particles as the source of minor particle ejection events

The post-impact velocity of any impactor depends on the properties of both the impactor and the target surface, as well as the complex accumulated effect of a range of impact parameters: speed, impact angle, impactor orientation or attitude, local gravity, local tilts, etc. The complexities of this interaction are typically reduced to a single parameter that defines the relationship between the initial and final velocity ($\mathbf{v_i}$ and $\mathbf{v_f}$, respectively) of the impactor, the effective coefficient of restitution,

$$\varepsilon_{eff} = |\mathbf{v_f}| / |\mathbf{v_i}| \qquad \text{eq. S3}$$

Bounces off the surface

Touchdown trajectory analyses of spacecraft on asteroid Itokawa (*45*) showed that low-speed impacts onto an asteroid surface result in high effective coefficients of restitution: 0.84 and 0.8, respectively. For a particle that re-impacts at a speed v_i = 30 cm s^{-1}, this translates to a launch speed of 25.2 and 24 cm s^{-1}, respectively. These speeds are commensurate with launch speeds of smaller particle events. Bouncing off a boulder on Bennu is feasible as more than 10% of its surface is covered by boulders > 4 m (*17*).

Ricochet and particle ejecta

We used numerical simulations of particle dynamics in microgravity (*90*, *91*, *47*) to obtain a better understanding of the interaction between an impactor and fine-grained material in the low-impact-speed (10's of cm s^{-1}) regime and low-gravity environment of a small asteroid. We use simulations as both of these conditions are difficult to reproduce in a laboratory environment.

Depending on the impact geometry and impact speed, ε_{eff} can range from virtually zero up to 0.8, with higher impact angles (with respect to the surface normal) leading to higher ε_{eff} (fig. S9, A and B). This effect is analogous to skipping stones on water. Furthermore, these simulations show that a 30-cm impactor can eject 2-cm particles with ejection speeds up to 20 cm s^{-1} (fig. S9C).

Meteor apparent entry velocity

The apparent entry velocity (V_∞), or atmospheric velocity, is derived from the following equation (*92*)

$$V_\infty = \sqrt{V_g^2 + V_E^2} \qquad \text{eq. S4}$$

where V_g is the geocentric velocity (6 km s^{-1} for Bennu) and V_E is the escape velocity of the Earth (11.2 km s^{-1}).

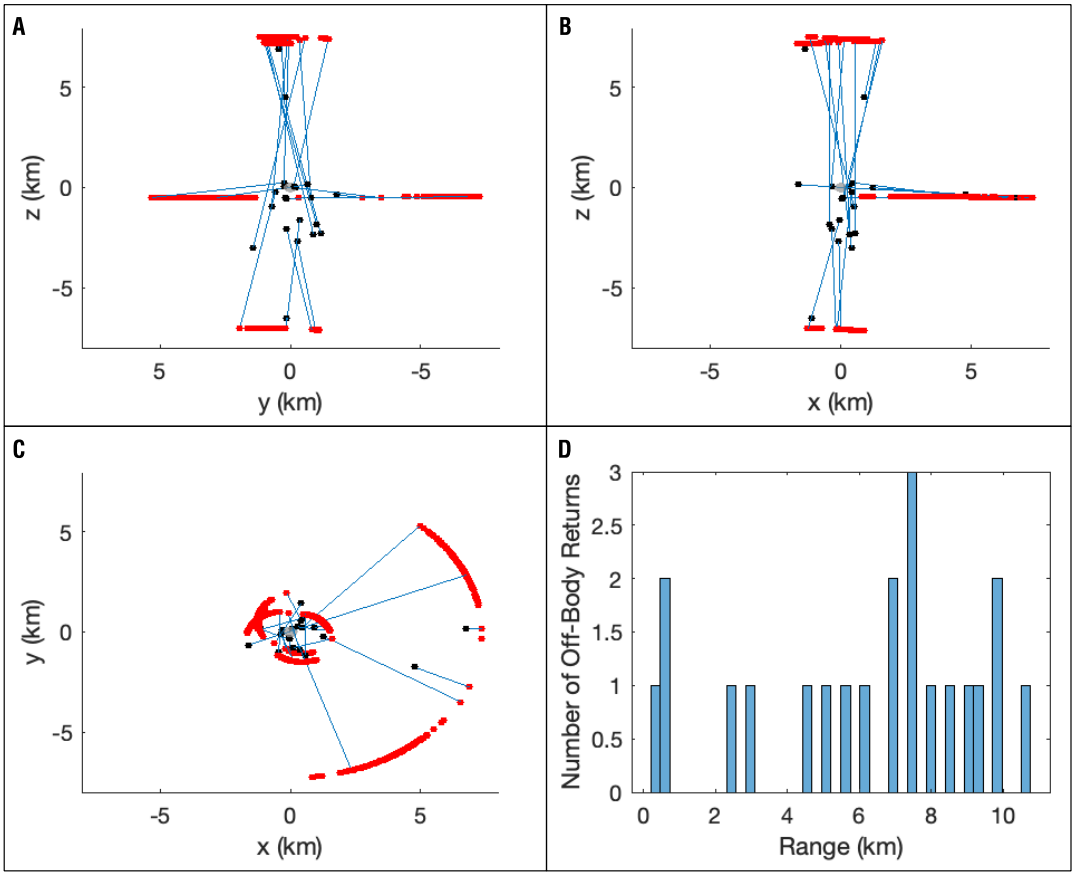

Fig. S1. Off-body returns from the OLA instrument. (**A** to **C**) Geometry of the 21 off-body lidar returns (black) in a Bennu (gray)–centered geometry. The spacecraft positions are shown in red for all returns and illustrate its trajectory relative to Bennu and the temporal locations of the 21 returns relative to on-body returns. (**D**) Range of off-body returns from Bennu's center of mass.

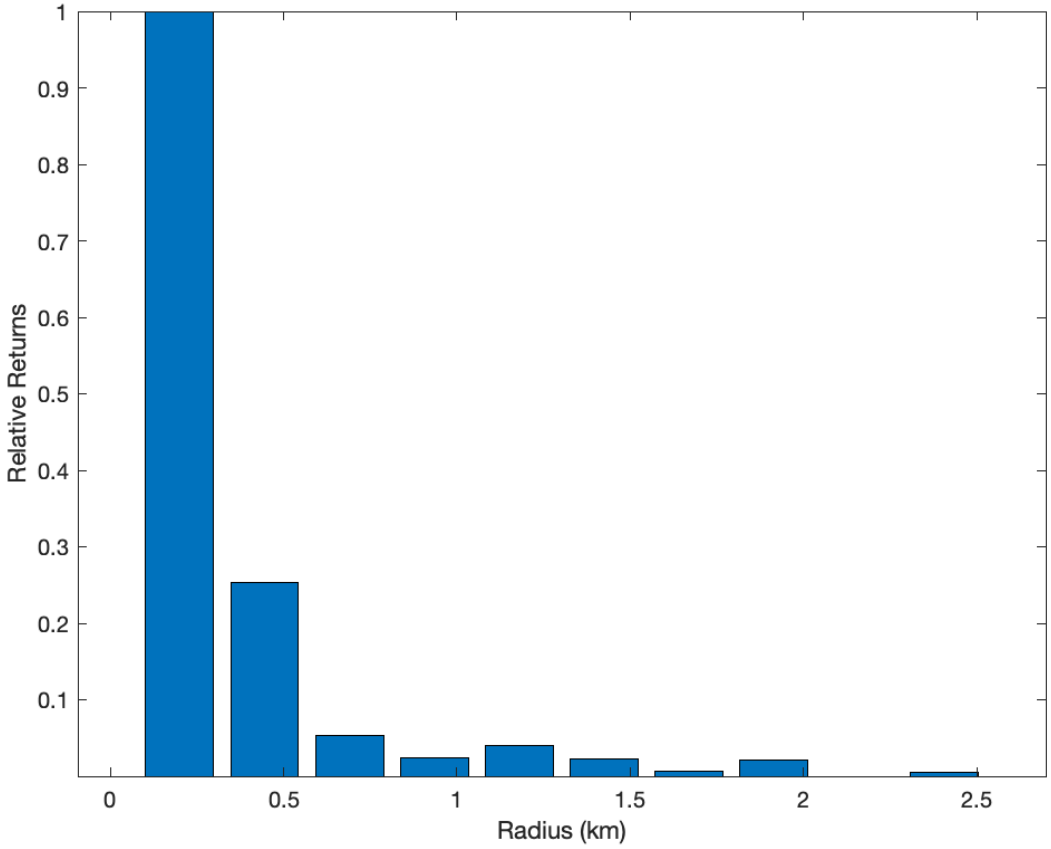

Fig. S2. Relative confidence of OLA off-body returns. The assessed relative confidence of the detections normalized to the largest bar and referenced to the radius from the center of Bennu.

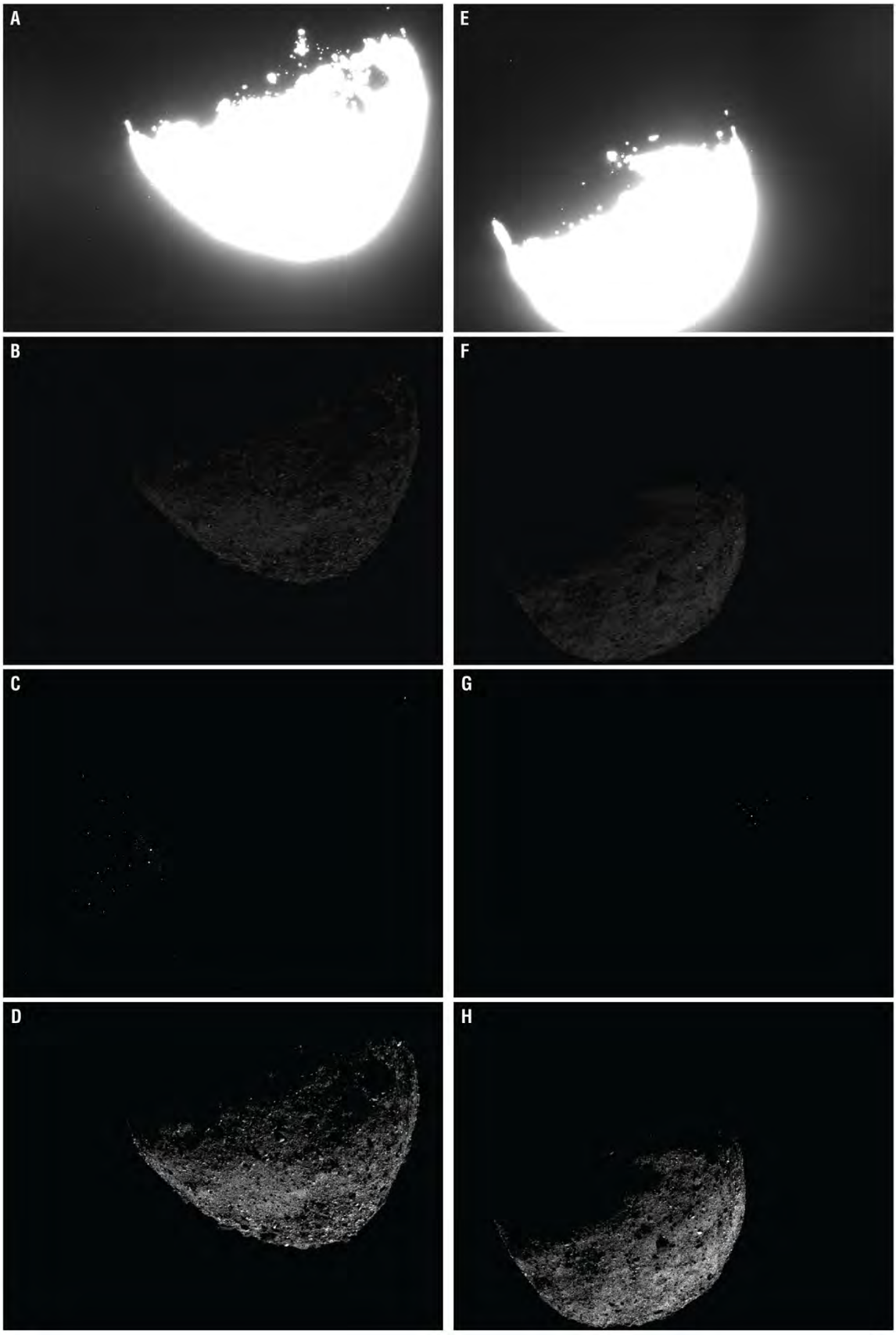
A
E
B
F
C
G
D
H

Fig. S3. Ejection event image processing. These NavCam 1 images show the steps to produce Fig. 1, A and C. Panels (A) to (D) are for 6 January, and panels (E) to (H) are for 19 January. (**A**) Original long-exposure image from 2019 January 6 20:56:18.792 UTC. (**B**) Original short-exposure image from 2019 January 6 20:56:11.433 UTC. (**C**) A median-filtered version of (A) that removes the signal of the asteroid and background stars and enhances the visibility of particles (see Production of NavCam 1 ejection event images). (**D**) DN histogram of the image in (B) is modified to set the background space to 0 DN while also making the darker regions of Bennu brighter. (**E**) Original long-exposure image from 2019 January 19 01:03:34.888 UTC. (**F**) Original short-exposure image from 2019 January 19 01:03:26.935 UTC. (**G**) As in (C), but for (E). (**H**) As in (D), but for (F).

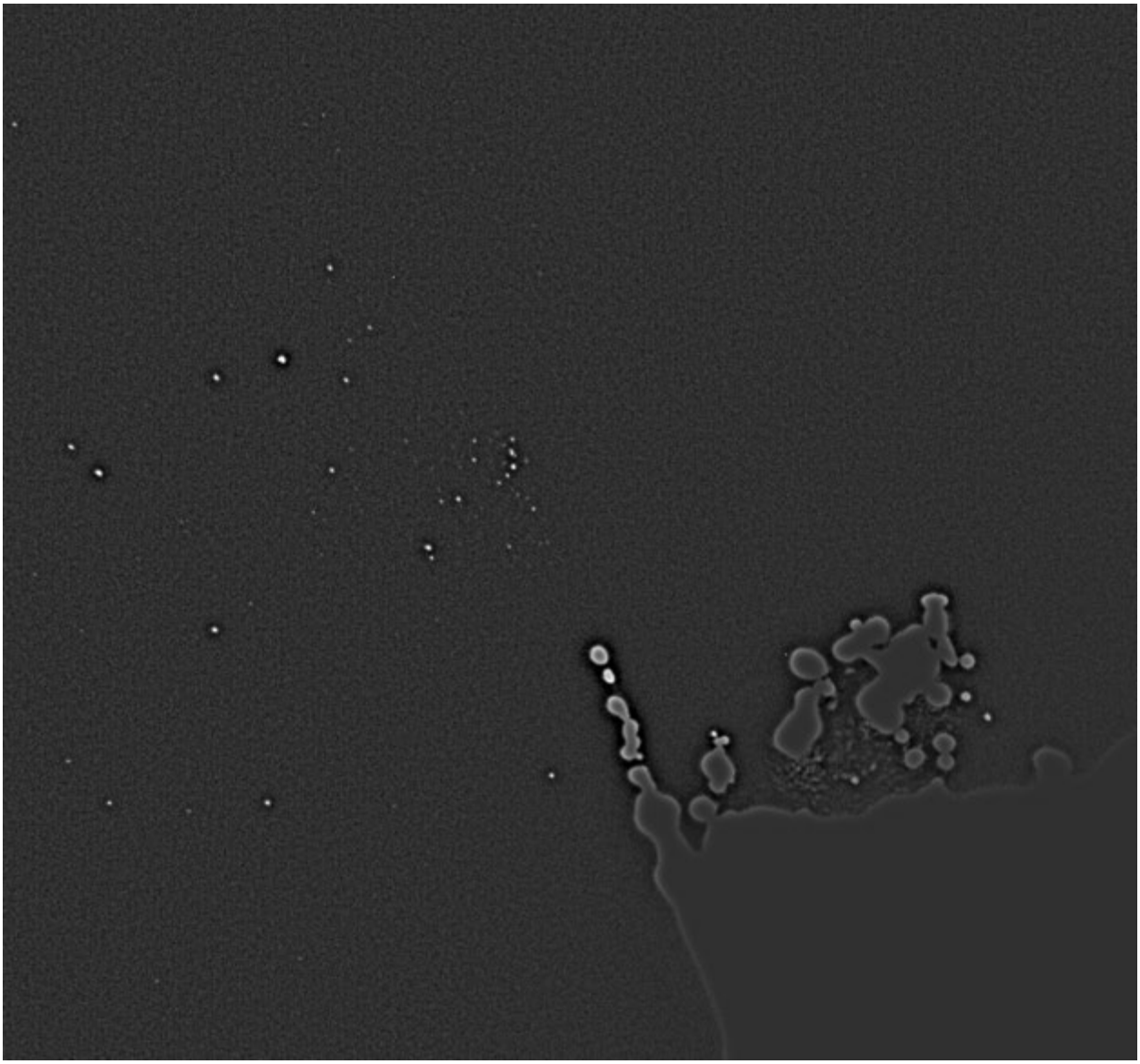

Fig. S4. Particle ejection on 11 February. This image was created from a long exposure, using the stray light reduction techniques described above. No short-exposure image was available close in time to the long-exposure image; thus, unlike in Fig. 1, A and C, Bennu is saturated in this image (lower right), and no surface detail is visible. The north pole is to the lower left on the asteroid, pointing into the image; the sub-observer latitude is –52°.

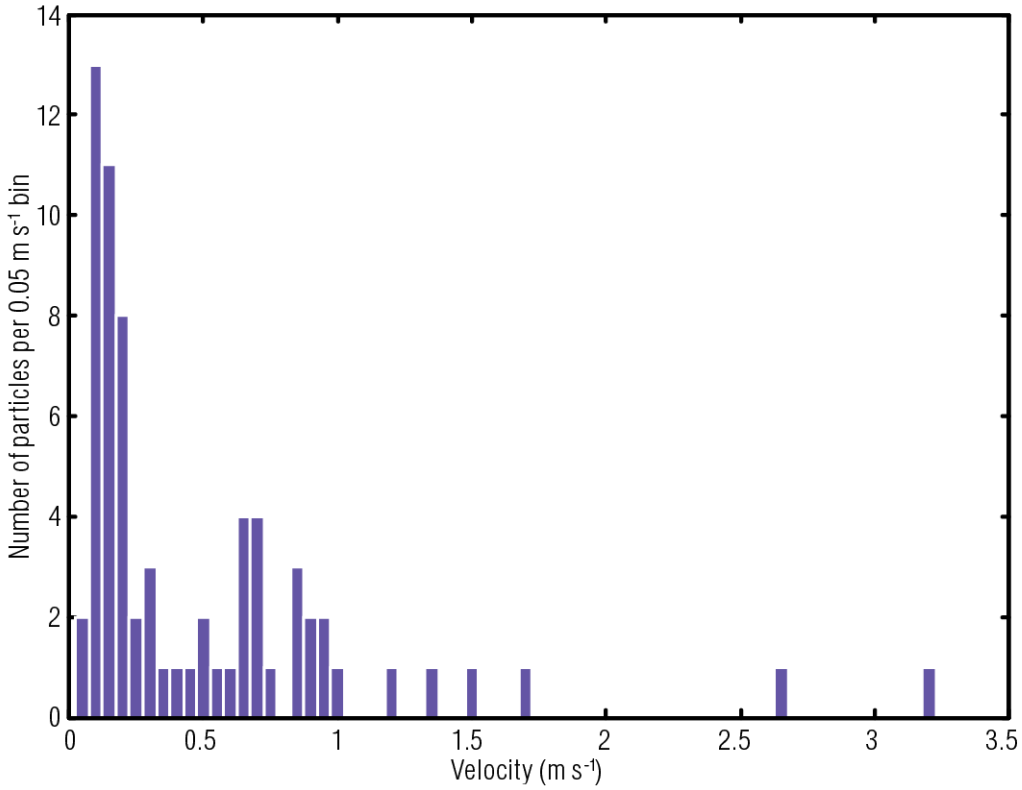

Fig. S5. Velocity histogram for the 6 January ejection event. Velocities were determined for 117 of the 200 observed particles from the 6 January event. The velocity distribution is a biased sample. Higher-velocity particles may have left the NavCam 1 field of view prior to imaging. Lower-velocity particles would have remained too close to Bennu to be observed. Each velocity bin (*x* axis) is 0.05 m s^{-1} wide.

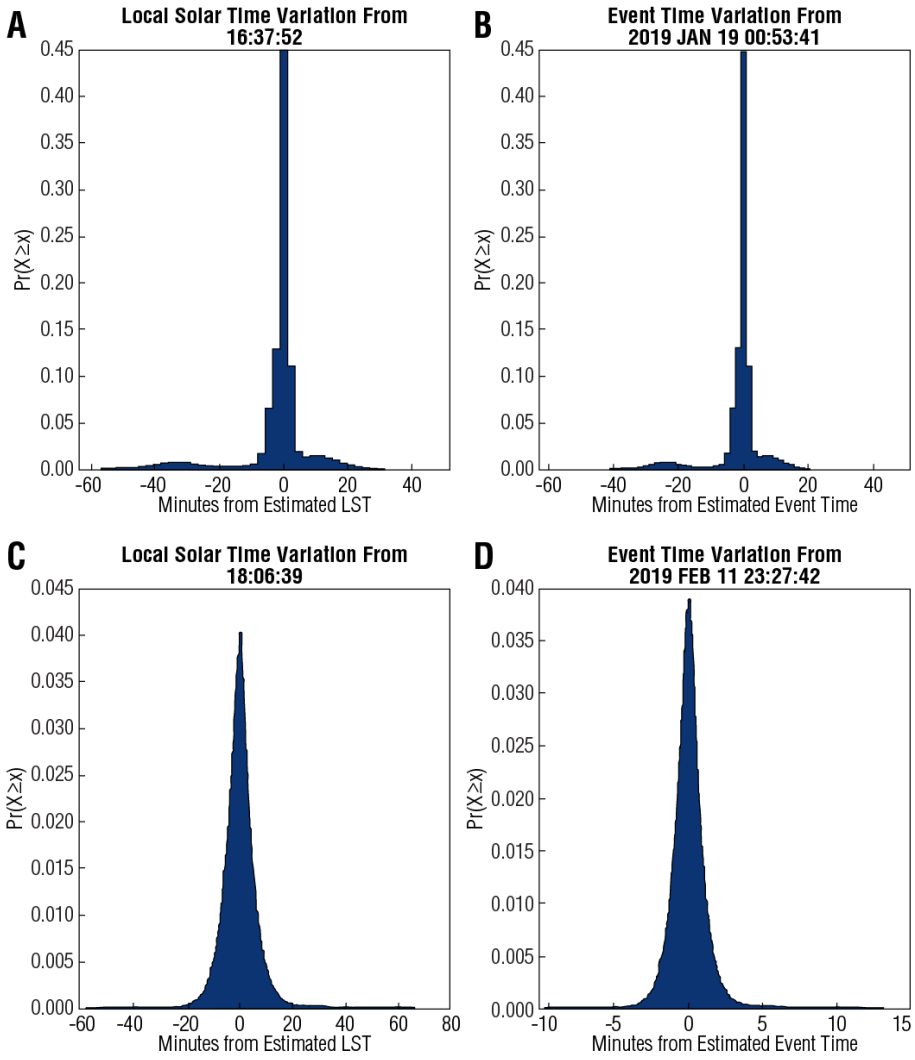

Fig. S6. Ejection time variation. (**A**) Time variation in Bennu LST minutes (each LST minute is ~10.8 SI seconds) for the 19 January event. (**B**) Time variation in SI minutes for the 19 January event. (**C** and **D**) As in (A) and (B), but for the 11 February event.

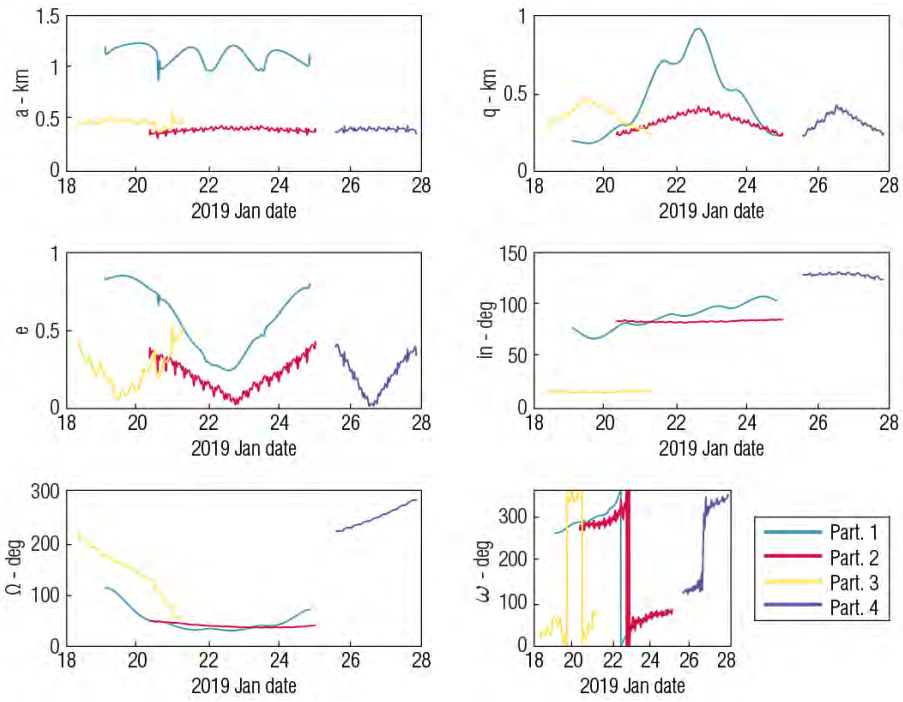

Fig. S7. Orbital element histories of particles 1 to 4. A pattern of initially decreasing eccentricity *e* and associated decrease in periapsis distance *q* is seen in all cases. After reaching low eccentricity, the argument of periapsis (ω) flips 180°, and the process reverses until impact. As predicted by classical perturbation theory, particle 3 has a low inclination and so Bennu's oblateness manifests in a receding longitude of ascending node (Ω). Particle 4 displays the converse behavior: $i > 90°$ with advancing Ω.

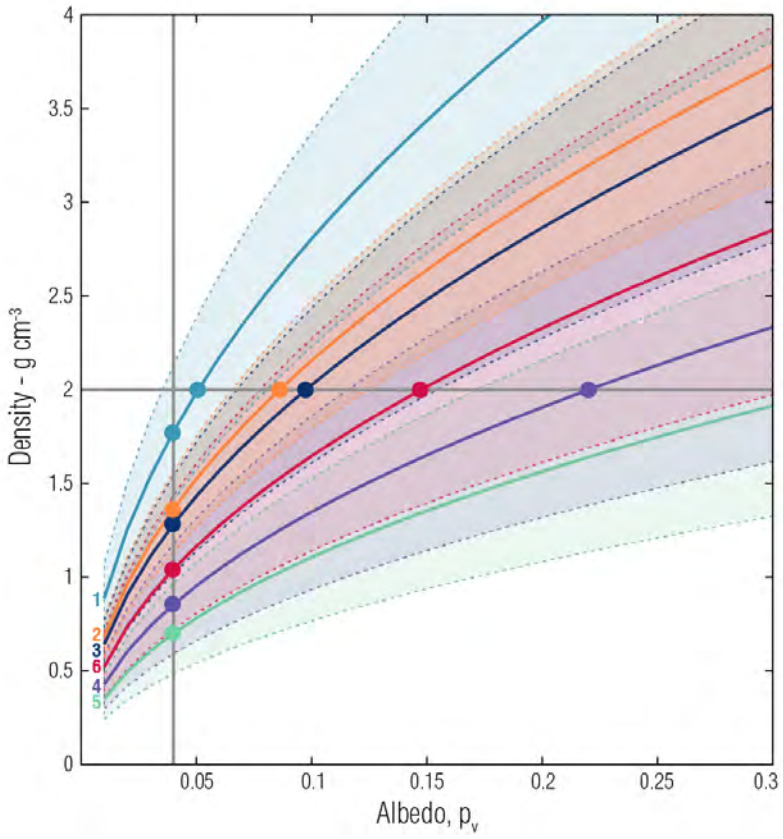

Fig. S8. Parameter space of albedo and bulk density for six gravitationally bound particles. Albedo-density curves are shown based on the estimates of area-to-mass ratios and absolute magnitude for particles 1 to 6 (indicated by numbers and line color; table S5), assuming spherical particles. Dashed curves and shaded regions indicate the 1σ uncertainty envelopes. Horizontal (density = 2 g cm^{-3}) and vertical (albedo = 0.04) gray lines are guides for the eye.

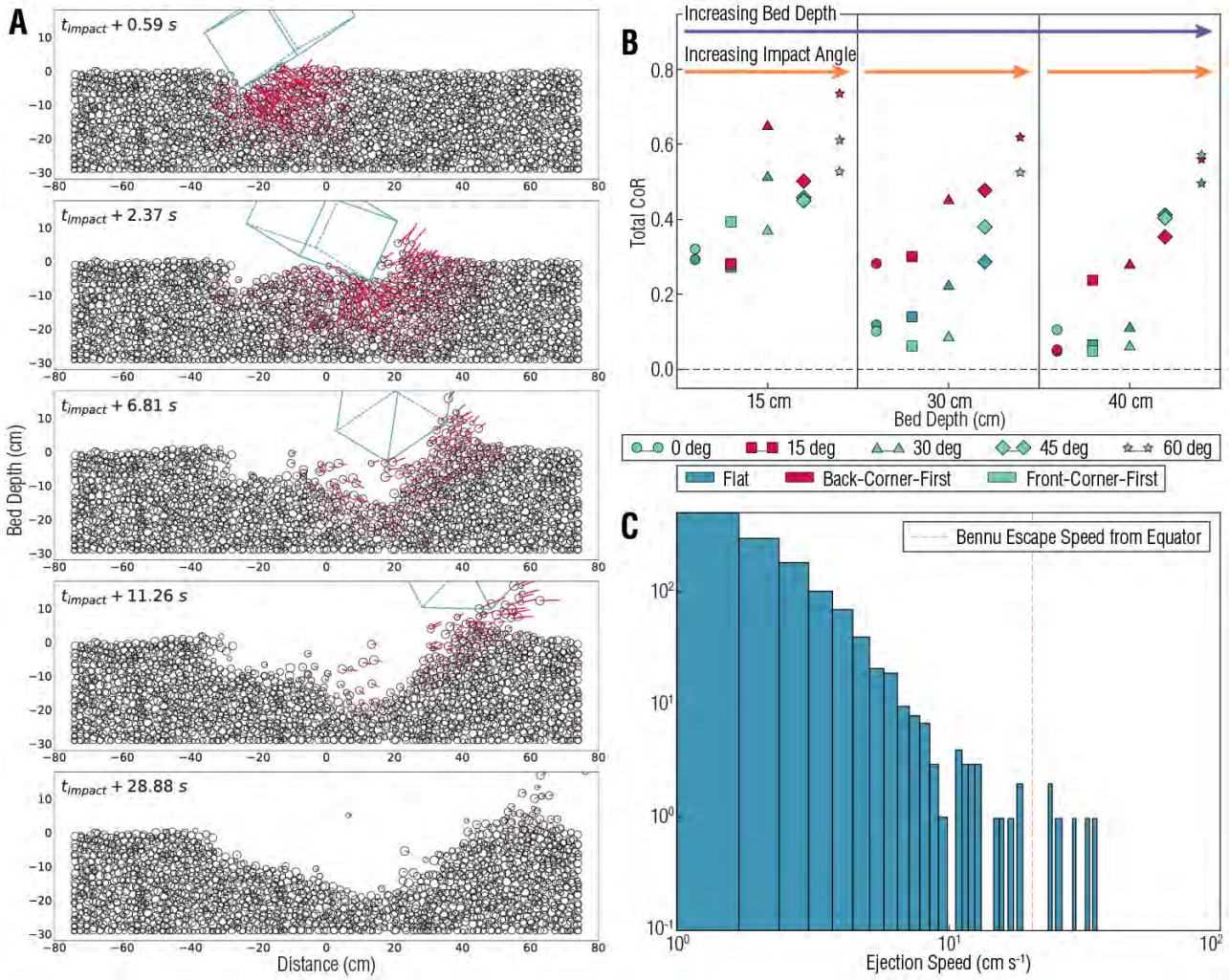

Fig. S9. Kinetic ejection of particles from the regolith surface. Panels (A) and (B) are adapted from (*47*), which studied the deployment of the MASCOT (Mobile Asteroid Surface Scout) lander [blue cuboid in (A)] on to the surface of asteroid Ryugu. The impact speed was 19 cm s^{-1}, and the impact geometry (impact angle and orientation of the lander) was varied. (**A**) A low-speed impact on to a fine-grained surface (surface grains had radii between 0.6 and 1.3 cm) can lead to the ricochet of the impactor, the launching of surface grains, and the formation of a shallow crater. (**B**) The effective coefficient of restitution (CoR) is highly sensitive to the angle of impact. An impact at larger angles (with respect to the surface normal) leads to larger post-impact velocities, with impact angles greater than 60° resulting in only a 20% reduction in the impactor's speed. [Credit: Adapted from Thuillet et al.] (**C**) An example of the distribution of launch speeds of ejected particles after an impact.

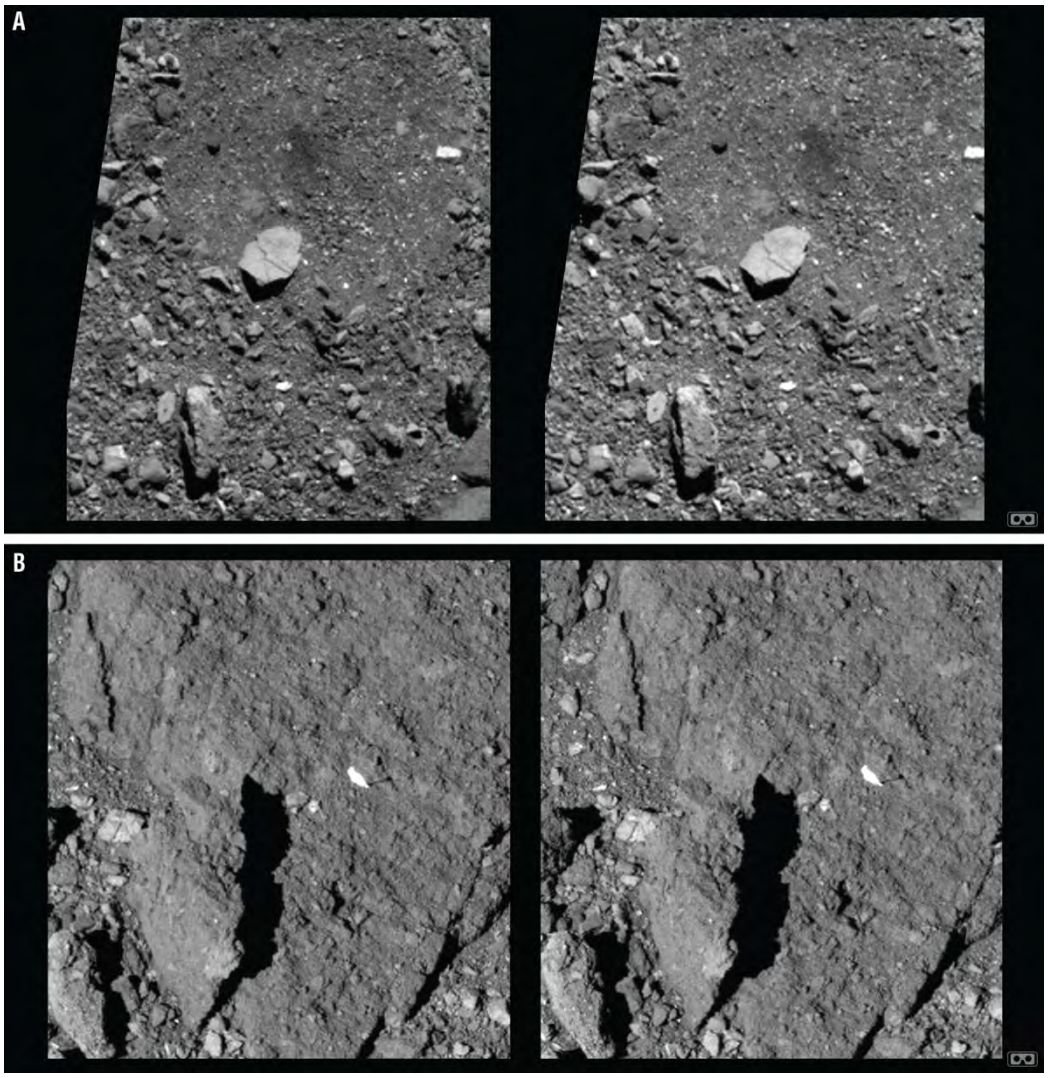

Fig. S10. Stereoscope version of the stereo pairs shown in Fig. 5. These stereo images are best viewed using a stereoscope. The left (right) image must be viewed by the left (right) eye. The sizes of the images conform to the format of the Brewster geometry.

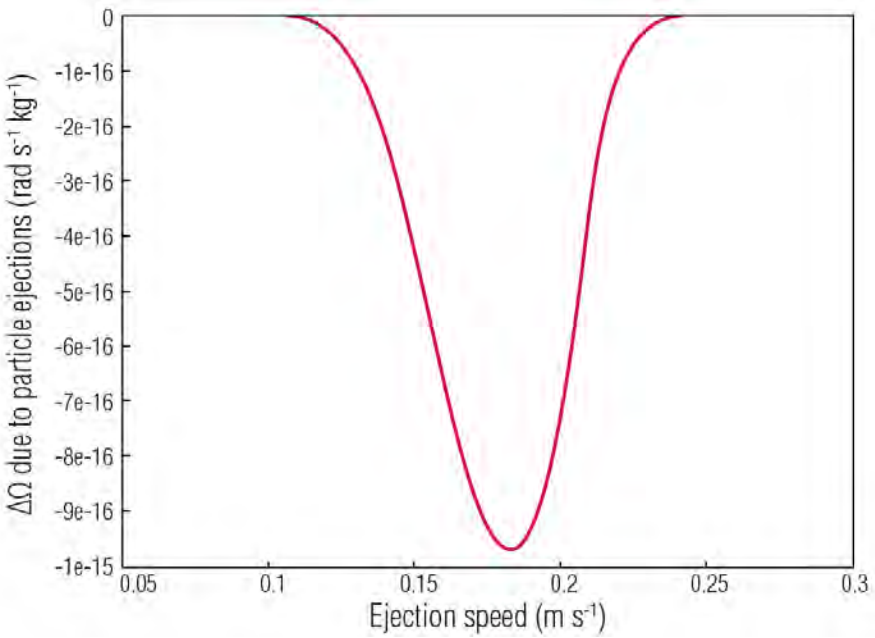

Fig. S11. Change in Bennu spin rate due to uniform ejection of particles at different surface ejection speeds. The net contribution can only slow the spin rate, and goes to zero when all particles uniformly escape. Computed using a 3-m-resolution shape model (*16*, *64*).

Table S1. Cadence of NavCam 1 imaging during Orbital A. The original cadence of NavCam 1 imaging was designed for optical navigation. These navigation images consisted of a short-long exposure pair at two offset pointings (OpNav1 and OpNav2). This set was repeated every 2 hours for the duration of the daily 16-hour observation windows. After the detection of particle ejections, the cadence was increased to once every 30 minutes starting on 11 January. The cadence was further refined on 28 January. Long-short exposure time pairs at two offset pointings were taken every 2 hours specifically for optical navigation. In between those navigation images, two long-exposure pairs were obtained every 20 minutes at a single nadir pointing. The times between each image had a variance of a few seconds.

Image #	**1**	**2**	**3**	**4**	**5**	**6**	**7**	**8**	**9**	**10**	**11**	**12**	**13**	**14**	**15**
	Dec 31 – Jan 10														
Previous image time (s)	6755	8	428	8	Repeat										
Exposure time (s)	0.0013	5.0002	0.0013	5.0002	Repeat										
Pointing	OpNav1	OpNav1	OpNav2	OpNav2	Repeat										
	Jan 11 – Jan 27														
Previous image time (s)	1356	8	428	8	Repeat										
Exposure time (s)	0.0013	5.0002	0.0013	5.0002	Repeat										
Pointing	OpNav1	OpNav1	OpNav2	OpNav2	Repeat										
	Jan 28 – Feb 18														
Previous image time (s)	1068	8	428	8	1042	137	991	137	991	137	991	137	991	137	Repeat
Exposure time (s)	0.0013	5.0002	0.0013	5.0002	5.0002	5.0002	5.0002	5.0002	5.0002	5.0002	5.0002	5.0002	5.0002	5.0002	Repeat
Pointing	OpNav1	OpNav1	OpNav2	OpNav2	Nadir	Nadir	Nadir	Nadir	Nadir	Nadir	Nadir	Nadir	Nadir	Nadir	Repeat

Table S2. Expanded data for the largest observed ejection events. Same as Table 1 but expanded to include the 6 and 19 January ejection event parameters for the initial near and far radiant solutions are shown. Uncertainties are discussed in the methods.

	January 6		**January 19**			**February 11**		
# of measured particles	124		93			60		
Velocity range (m s^{-1})	0.07 to 3.3		0.06 to 1.3			0.07 to 0.21		
Diameter (cm, ±1σ)	<1 to 8±3		<1 to 7±3			<1 to 7±3		
Event energy (mJ, ±1σ)	270 (+150, –225)		100 (+50, –85)			8 (+4, –7)		
	Near Radiant	Far Radiant	Near Radiant	Far Radiant	OD Radiant	Near Radiant	Far Radiant	OD Radiant
Latitude (deg, ±3σ)	–74.95 (+12.65, –2.79)	–57.30 (+1.49, –17.49)	46.64 (+2.85, –5.97)	23.16 (+5.70, –3.78)	20.63 ±0.30	10.95 (+7.92, –6.55)	25.23 (+11.34, –9.83)	20.68 ±0.37
Longitude (deg, ±3σ)	325.32 (+18.91, –10.28)	343.67 (+3.80, –14.73)	327.69 (+4.59, –3.46)	334.15 (+3.73, –3.87)	335.40 ±0.09	59.73 (+8.12, –7.52)	60.07 (+8.19, –8.02)	60.17 ±0.08
Body-fixed vector (km, ±3σ)	X = 0.0510 Y = –0.0353 Z =–-0.2307	X = 0.1227 Y = –0.0359 Z = –0.1991	X = 0.1364 Y = –0.0863 Z = 0.1709	X = 0.2038 Y = –0.0987 Z = 0.0969	NA	X = 0.1266 Y = 0.2184 Z = 0.0486	X = 0.1079 Y = 0.1885 Z = 0.1016	NA
Local solar time (±3σ)	15:22 (+01:06, –00:36)	16:35 (+00:06, –01:05)	16:10 (+00:09, –00:06)	16:36 (+00:04, –00:06)	16:38:01 ± 23 s	18:12 (+00:24, –00:22)	18:13 (+00:24, –00:23)	18:05:31 ± 22 s
Event time (UTC, ±3σ)	20:50:28 ± 47 s	20:50:28 ± 47 s	00:53:55 ±40 s	00:53:55 ±40 s	00:53:41 ± 4 s	23:28:35 ±38 s	23:28:35 ±38	23:27:28 ± 6 s

Table S3. Approximate mass, volume, and energy for the largest particle events. Only particles with measured velocities and photometry are included. No attempt has been made to debias the event populations for particles not imaged due to their faintness or proximity to Bennu. A linear phase function of 0.018 mag per degree of phase angle and density of 2 g cm^{-3} was assumed for all particles in this table.

Event date	Sun-Bennu Distance (au)	# of particles	Velocity range ($m\ s^{-1}$)	Mass (g)				Volume (cm^3)				Energy (mJ)			
			Albedo =	0.033	0.044	0.070	0.150	0.033	0.044	0.070	0.150	0.033	0.044	0.070	0.150
Jan 6	0.897	124	0.07-3.3	2700	1800	900	280	1350	880	440	140	420	270	135	45
Jan 19	0.899	93	0.06-1.3	1000	600	300	100	610	400	200	60	150	100	50	15
Feb 11	0.933	60	0.07-0.21	1000	700	300	100	670	430	220	70	12	8	4	1

Table S4. Approximate orbital elements of six particles. The orbital elements are orbital period P, semimajor axis a, eccentricity e, periapsis distance q, apoapsis distance Q, inclination i, and longitude of ascending node Ω. The epoch of osculation is near the middle of the particle lifespan. These orbits evolve rapidly under perturbations from radiation pressure and Bennu's complex gravitational potential, so these elements are only a rough guide as to the shape and orientation of the orbit. The reference frame for i and Ω places the Sun on the z axis. Bennu's north pole $\hat{n}$ is in the x-z plane near the z axis and the y axis in the direction of $\hat{x} \times \hat{n}$, roughly in the direction of Bennu's heliocentric velocity.

No.	***P* (h)**	***a* (km)**	***e***	***q* (km)**	***Q* (km)**	***i* (deg)**	**Ω (deg)**
1	29.66	1.12	0.36	0.72	1.52	96.42	34.31
2	7.1	0.43	0.04	0.41	0.45	82.44	38.39
3	8.72	0.5	0.09	0.45	0.54	15.34	155.47
4	6.23	0.4	0.05	0.38	0.42	127.84	246.54
5	4.68	0.33	0.37	0.21	0.45	32.37	223.53
6	20.69	0.88	0.9	0.09	1.68	17.46	80.64

Table S5. General characteristics of six particles, derived from photometric and trajectory fits. The absolute magnitudes are derived from the fitted linear phase functions (for particles 1 to 3) or the mean linear function (for particles 4 to 6) of 0.018 mag per degree of phase angle. The cross-sectional area-to-mass ratios (AMRs) and AMR-derived diameters are from orbit solutions. The diameter estimate assumes a spherical particle with density 2 g cm^{-3}. Ejection velocity is inertial, relative to Bennu.

Catalog number	Absolute magnitude (mag)	Cross-sectional AMR ($\times 10^{-3}$ m^2 kg^{-1})	Approx. diameter from AMR (cm)	Ejection Time	Ejection LST (h)	Ejection velocity (cm s^{-1})	Life-span (h)
1	$42.8^{-0.5}_{+0.4}$	47.1 ± 0.1	2	2019-Jan-19.0	11.8	19.0	140
2	$41.6^{-0.4}_{+0.3}$	36.1 ± 0.1	2	2019-Jan-20.3	15.5	16.5	113
3	$42.7^{-0.5}_{+0.4}$	62.7 ± 0.4	1	2019-Jan-18.3	3.2	16.3	71
4	$43.3^{-0.8}_{+0.7}$	85.1 ± 0.5	1	2019-Jan-25.6	2.0	16.0	55
5	$43.7^{-0.8}_{+0.7}$	164 ± 78	<1	2019-Jan-18.2	15.7	15.3	3.6
6	$39.5^{-0.8}_{+0.7}$	17 ± 10	3-10	2018-Dec-10.1	20.4	17.9	20

Data S1. Pixel coordinates, times, observing geometries, velocities, and apparent magnitudes for one image in each of the largest observed ejection events. Particles without OD solutions use the mean value of the observing geometries and velocities. Also provided are photometric data for representative gravitationally bound particles 1 to 6.